TECHNISCHE UNIVERSITÄT WIEN
Vienna University of Technology

Design and Characterisation of 3D-Printed Magnetic Field Sensors

DIPLOMARBEIT
der Technischen Universität Wien

Ausgeführt am Institut für Sensor und Aktuatorsysteme der Technischen Universität Wien
in Kooperation mit dem Zentrum für Integrierte Sensorsysteme der Donau-Universität Krems

unter der Anleitung von

Ao.Univ.Prof. Dipl.-Ing. Dr.techn.
Franz Keplinger

und

Univ.Lektor Mag.rer.nat. Mag.rer.nat. Dr.techn.
Michael Stifter

durch
Matthias Kahr
Matr.-Nr. 0925276
Wien, im November 2017

There is beauty in simplicity. And it's even more satisfying when this beauty condenses out of complexity.

(Helen Czerski, Storm in a Teacup: The Physics of Everyday Life, 2016)

Danksagung

An dieser Stelle möchte ich mich bei all jenen Personen bedanken die mich direkt und auch indirekt bei der Durchführung dieser Diplomarbeit begleitet haben. Dank geht an Prof. Franz Keplinger, der mir sowohl den Freiraum bei der Durchführung bot als auch mit Expertise zur Vollendung der wissenschaftlichen Arbeit zur Seite stand. Vielen Dank auch an Dr. Andreas Kainz, der akribisch meine Arbeit korrigierte und mir Einblicke in die Welt ästhetisch wohldefinierter Sätze bot.
Im Besonderen möchte ich mich bei Dr. Michael Stifter, Dr. Wilfried Hortschitz und Dr. Harald Steiner, dem "Wiener Neustädter-Team" bedanken, die mit mir dutzende Diskurse über mögliche Versuchsdurchführungen und deren Interpretation geführt und sich weiters als würdige Tischfußballspieler erwiesen haben.
Bei Dr. Artur Jachimowicz möchte ich mich für die Versuche in der Aufdampfanlage zur Beschichtung der Sensoren bedanken.
Desweiteren möchte ich mich bei Günter Hammer für Diskussionen abseits des Studiums und die entspannte Raumteilung während meiner schreibintensiven Phase bedanken.
Dank geht vor allem an meine Familie, die mich durch all die Hochs und Tiefs begleitet und das Studium ermöglicht hat.
Im Speziellen möchte ich mich bei meiner Freundin Anna Larcher, MA MA für ihr großes Verständnis während dieser arbeitsintensiven Zeit und ihre motivierenden Phrasen wie "Alles geht zu Ende" bedanken.

Kurzfassung

In dieser Arbeit werden 3D gedruckte Magnetfeld Sensoren, die auf dem Effekt der Lorentz Kraft beruhen, untersucht. Der 3D-Druck ermöglicht eine schnelle und kostengünstige Herstellung von dreidimensionalen Werkstücken und kann zu beschleunigten Testphasen von Designs in der MEMS Entwicklung führen. Vorteile von "Rapid Prototyping" als Beurteilungsmethode werden in dieser Arbeit diskutiert, um die Funktionalität für entworfene Mikrostrukturen vor der Anwendung kostspieliger traditioneller MEMS-Technologie zu demonstrieren.
Das Messprinzip basiert auf der Modulation von Lichtfluss, welches durch eine relative Verschiebung von zwei speziell strukturierten Masken ermöglicht wird. Eine Maske, welche Teil einer beweglichen Masse ist und durch Lorentz Kräfte ausgelenkt werden kann, wird einer stationären Maske gegenüberliegend ausgerichtet. Untersucht werden zwei verschiedene Designs, welche sich durch die Art der Magnetfeldmessung geometrisch unterscheiden. Beide Designs besitzen eine horizontal auslenkbare Masse, um den Lichtfluss zu modulieren. Der erste Prototyp besitzt einen sensitiven Bereich auf der Masse, der eine ausgeprägte Eigenfrequenz für horizontale Schwingungen aufweist. Der zweite Prototyp besitzt einen elastischen Mechanismus (engl. 'complient mechanism'), bei dem die Bewegung von magnetfeldsensitiven vertikal schwingenden Balken durch gekrümmte Federn in eine horizontale Bewegung der Masse umgeleitet wird.
Zusätzlich werden auftretende Probleme während der Werkstückanfertigung, wie unter anderem der Einfluss von Wachsrückständen auf das Verhalten der Prototypen und die Schwierigkeit eine metallische Beschichtung aufzutragen, behandelt. Um die Sensitivität der Sensoren zu bestimmen und generell reproduzierbare Messungen durchführen zu können, wurde eine Vorrichtung entwickelt, die ein schnelles und leichtes Austauschen von Magneten mit unterschiedlichen Feldstärken ermöglicht. Messergebnisse der Sensitivitäten ergaben 146 mV/T für Prototyp 1 und 253 mV/T für Prototyp 2.
Weiters wurden die Effekte von Beugungerscheinungen sowie der Einfluss von fehlerhaft ausgerichteten Masken untersucht. Beugung konnte durch Masken mit größeren Aperturen minimiert und die Reproduzierbarkeit der Messungen durch ideal ausgerichteten Masken verbessert werden.
Die komplexe Geometrie des zweiten Prototypen wird mit FEM Simulationen untersucht, um das Schwingverhalten der Masse in einem homogenen und inhomogenen magnetischen Feld zu verstehen. Dazugehörige Resultate der optischen Messung korrelieren sehr gut mit den Ergebnissen der Simulation.
Die ständige Weiterentwicklung des 3D-Drucks ermöglicht eine laufende Verbesserung des "Rapid Prototyping" Ansatzes im Sinne von kleineren druckbaren Sensoren, verbesserter Druckgenauigkeit, Einsatz neuer Materialien und möglicherweise weiter sinkenden Produktionskosten.

Abstract

Lorentz force based 3D printed magnetic field sensors are investigated in this thesis. The sensing principle is based on the detection of modulated light flux from two stencil masks by relative in-plane movement. Hence, one mask is part of the moveable mass which is actuated by Lorentz forces, whereas the second grating is aligned on the opposite side and fixed onto a stationary frame. Two unique designs are proposed, both are exhibiting the in-plane deflectable mass for light modulation but they differ in the sensing approach. The first prototype exhibits the effective sensing area on the mass and is designed with a distinct eigenfrequency yielding in-plane deflections, whereas the second prototype features a complient mechanism. This mechanism consists of curved springs that transform out-of-plane oscillations from sensing cantilevers into an in-plane movement of the mass.

Advantages of 3D printing technologies in terms of fast design and accelerated testing phases as well as the possibility of creating printed 'real' three dimensional MEMS structures are discussed. Therefore, this work focuses on rapid prototyping which is an effective assessment tool to demonstrate working principles for designs before initiating costly traditional MEMS technology.

The above mentioned prototypes are tested for their functionallity, investigation of ocurring problems during manufacturing such as the impact of wax residues and the difficulty of applying conductive coatings onto the surface were conducted. Further, a mounting device is designed to easy exchange magnets with different strength to characterise the sensors' sensitivity. Measured sensitivities for prototype 1 and prototype 2 are 146 mV/T and 253 mV/T, respectively.

The effect of light diffraction and rotational misalignment between both masks are studied in form of simulations and measurements. Diffraction was reduced by introducing masks with bigger aperture width. Due to the complex geometry of the prototype featuring the complient mechanism, additional FEM simulations have been realised, studying the structures deflection in a homogenous and inhomogenous external magnetic field, hence affirming the results from the optically measured light flux.

Ongoing development on the 3D printing market enables potential for further enhancements for rapid prototyping such as smaller printable sensor designs, new materials with unique properties, higher printing accuracy and probably even cheaper manufacturing costs.

Contents

Danksagung **iv**

Kurzfassung **v**

Abstract **vi**

1 Introduction **1**
1.1 Objective and Structure of the Thesis 2

2 Sensor Principle **5**
2.1 Sensor Design 5
2.2 Harmonic Oscillator 7
2.2.1 Simple Harmonic Oscillator 7
2.2.2 Damped Harmonic Oscillator 8
2.2.3 Driven Damped Harmonic Oscillator 10
2.3 Quality Factor 12
2.4 Lorentz Force Actuation 13
2.5 Sensitivity S 13
2.6 Thermomechanical Noise 15

3 Optoelectronics and Amplifier **19**
3.1 Photodetector 19
3.2 Readout Circuit 20

4 Prototypes Fabrication and Characterisation **21**
4.1 Manufacturing Technology 21
4.1.1 3D Printing Technology for MEMS 21
4.1.2 Prototype Fabrication 25
4.1.3 Surface Coating 25
4.1.4 Glass Wafer Fabrication, Mask Alignment and Diffraction Phenomena 29
4.2 FEM Analysis 30
4.3 Measurement Settings 32
4.4 Out-Of-Plane Magnetic Field Sensor 34
4.4.1 Comsol Simulation 34
4.4.2 Sensitivity Measurement 36
4.4.3 Effect of Different Aperture Width 41
4.4.4 Effect of Mask Alignment 42
4.4.5 Temperature Dependence 44
4.5 In-Plane Magnetic Field Sensor 46
4.5.1 Measurement Results - Sensitivity 47

4.5.2 Comsol Simulation 50

5 Conclusion **55**

Appendix A Neodymium Magnets **57**

Appendix B Wax Residues **58**

Appendix C Measurement Setup - Field Distribution between Pole Shanks **59**

References **61**

Code of Conduct **65**

1 Introduction

Magnetic sensing techniques combine the fields of physics and material science and are extensively used in analysing and controlling important functions of today's society. For example, reliability of noncontact switching with magnetic sensors sets high safety standards for airplanes. Magnetometers enable accurate measurement of the position at engine crankshafts and wheel brakes. Furthermore, increased productivity in factories is achieved due to stability and low cost of magnetic sensors [1].

A short survey of currently existing magnetometers shall introduce their tremendous diversity and applications. The most sensitive magnetic field sensors are based on flux quantisation in superconducting loops and the Josephson effect, achieving high resolutions in the order of fT and lower. Those Superconducting Quantum Interference Devices (SQUID) are mainly used in biology, medicine (neuromagnetism) and geology applications. Unfortunately, the commercial use of SQUID-based applications is restricted due to high costs, requirement of a sophisticated infrastructure (cooling with helium, electromagnetic shielding) and high power consumption [2].
Another type of magnetic field sensors using the Hall effect, is based on low cost standard CMOS technology and are designed to detect magnetic fields larger than 10 nT [3]. Hall effect sensors are used for measuring linear and angular position, velocity, rotational speed and are suitable for both constant or varying magnetic fields. However, they require compensation circuits to counterbalance thermally induced drifts.
Search coil magnetometers measure varying magnetic fields based on Faraday's law of induction. The typical size of these sensors varies from a few centimetres up to a metre, with higher sensitivities for larger sensor systems. Applications are provided for non-destructive testing, traffic controls, space research on plasma physics [4].
A conventional sensor for measuring static or low-frequency magnetic fields in applications such as magnetotellurics, compass navigation systems, airborne magnetic field mapping or detecting submarines, is the fluxgate magnetometer. Fluxgates are sensitive to both the field direction and the field magnitude, exhibiting resolution limits below $1\,\mathrm{pT}/\sqrt{\mathrm{Hz}}$. Complex fabrication of the magnetic core (e.g. ultrasoft amorphous cobalt alloy wire, [5]) and coils are major disadvantages.
Magnetometers based on a change in their electrical resistance are classified as magnetoresistive sensors. The classical type of those sensors are based on the anisotropic magnetoresistive (AMR) effect that occurs in ferromagnetic transition metals. Their electrical resistance depends on the angle between the direction of magnetisation and the electrical current. An external magnetic field alters the magnetisation, thus, causing a variation of the electrical resistance. A major drawback is the sensor's saturation already at small magnetic fields (several mT), hence depending on complex resetting procedures. Magnetoresistive sensors are used for magnetic heads in hard disks, vehicle detection and car speed monitoring, pneumatic cylinder position sensing, crankshaft position sensors, current detection, and noiseless locking

mechanisms [2]. Beside the aforementioned AMR there exist also other forms of magnetoresistance. The giant magnetoresistance (GMR) is based on multilayer structure of thin films, yielding a higher resistance change; the tunneling magnetoresistance (TMR) is based on quantum tunneling of electrons between thin insulators; the colossal magnetoresistance (CMR) is based on a change of nonmagnetic insulators to ferro-magnetic conductors at relatively large fields ($\sim$ 1T); the extraordinary magnetoresistance (EMR) based on additional conducting particles in the semiconducting material increasing concentrations in the current density [6].
Magnetometers based on microelectromechanical systems (MEMS) mostly based on the Lorentz force which is generated by the interaction between an electrical current and an external magnetic field. The Lorentz force causes an oscillation of the MEMS which is increased at resonance (MEMS excited with AC within a static external magnetic field). It is measured using capacitive, piezoresistive and optical sensing techniques. MEMS devices are composed by mechanical and electrical components with advantages such as small size, low power consumption, high sensitivity and reduced fabrication cost [7]. Table 1 summarises some recent MEMS magnetic field sensors and their characteristics.

Sensor	**Size (µm × µm)**	f_0 **in kHz**	Q	S
Herrera-May et al. [8]	400 × 150	136.52	842	403 mV/T
Langfelder et al. [9]	89 × 868	28.3	327.9	150 µV/µT
Laghi et al. [10]	282 × 1095	19.95	2500	0.85 V/mT
Minotti et al. [11]	1700 × 750	20	460	0.75 zF/(nT mA)
Park et al. [12]	3000 × 3000	0.36	116	62 mV/µT

Table 1: This table summarises characteristics of recent MEMS magnetic field sensors based on Lorentz force, where f_0 is the sensor's natural frequency, Q is the quality factor and S is the sensitivity. The data is extracted from [7].

A general introduction and review about micromachined resonators can be found in [13], whereas a more profound review about resonant magnetic field sensors is provided by [2] and [7].

1.1 Objective and Structure of the Thesis

The thesis is investigating 3D printed MEMS magnetometers with optical readout, demonstrating their functionality and discussing the advantage of low-cost state-of-the-art 3D printing technology in terms of rapid prototyping.
The thesis is structured as follows: Section 2 describes the sensing principle and designs in more detail and introduces fundamentals such as the harmonic oscillator, Lorentz force actuation, sensitivity and thermomechanical noise. Section 3 presents the working principle of a transimpedance amplifier and the chosen optoelectronic

components for the measurements. In Section 4, the potential of 3D printing technology, prototype fabrication and measurement results are discussed. This part provides further insight of occurring problems, fabrication limitations and how to adapt and improve the measured output signals. Finally, Section 5 summarises this work and proposes further methods to obtain a better understanding of 3D printing technologies and materials behaviour.

2 Sensor Principle

The general idea of the sensor consists of a three-dimensional (3D) printed mechanical transducer, an LED and a photodiode PD. The PD receives modulated light flux from two stencil masks by relative in-plane movement according to the shading by both gratings. Therefore, one mask is part of a moveable mass, which is actuated by Lorentz forces, whereas the second grating is aligned on the opposite side and fixed to the structure's stationary frame as depicted in Fig. 1. Those masks feature vapor deposited Cr arrays of apertures available with different aperture width. The PD placed at one side of the apertures measures the transmitted light intensity [14]. The signal is amplified with a transimpedance amplifier and acquired with a lock-in amplifier. The whole structure, including the stationary outer frame and the spring suspended mass is 3D printed in acrylic resin with Multijet Modeling technology. The glass chips are glued onto the 3D printed transducer with an instant adhesive. Major challenges in the alignment process of the glass masks are discussed in Subsection 4.1.4.

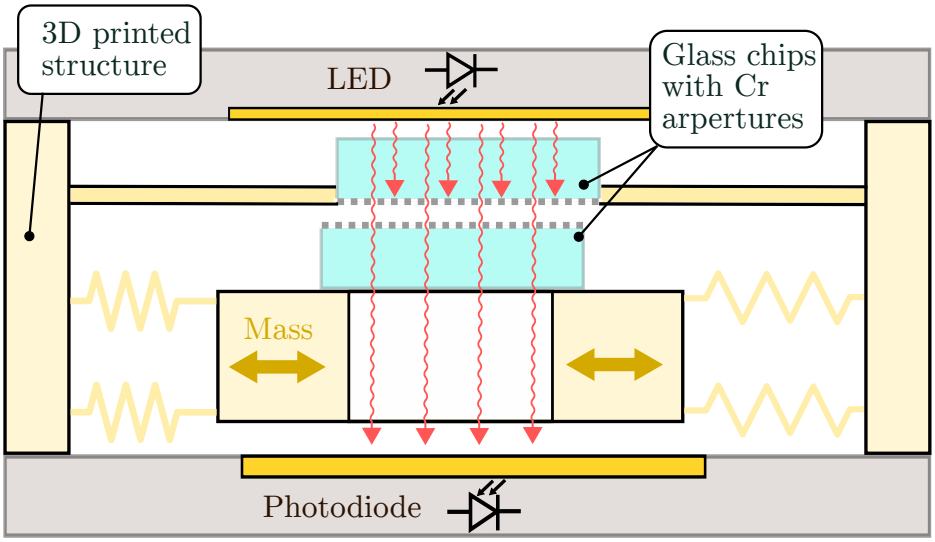

Figure 1: Schematic cross section of the sensor light modulation principle.

2.1 Sensor Design

Two unique designs for Lorentz force based magnetometers are proposed in this thesis (see Fig. 2). Both designs are 3D printed to allow for rapid prototyping and the possibility of fabricating complex truly 3D structures as in contrast to MEMS fabricated with conventional technologies.
The idea for the design and sensing principle of the out-of-plane magnetic field sensor is based on [15]. A magnetic field perpendicular to the current carrying moveable

Out-of-plane magnetic field sensor:

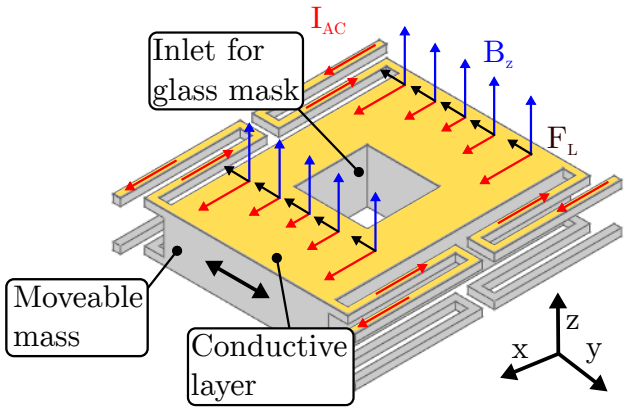

(a)

In-plane magnetic field sensor:

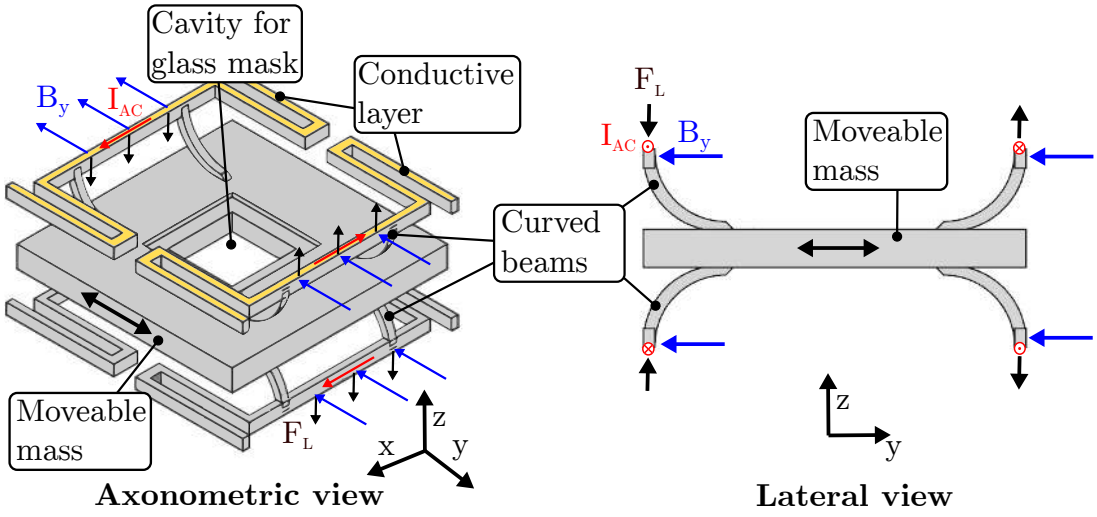

(b)

Figure 2: CAD schematic of the out-of-plane magnetic field sensor (a) and the in-plane magnetic field sensor (b). The terms 'out-of-plane' and 'in-plane' denotes the direction of the external magnetic field pointing perpendicular and lateral to the structures mass, respectively. The representation of the outer frame is omitted for the sake of clarity.

mass introduces a force which induces an in-plane deflection.

The in-plane magnetic field sensor depicted in Figure 2b benefits from the 3D printing technology. Curved beams transform the out-of-plane deflection of the current carrying cantilevers into an in-plane movement of the mass. This is achieved by a curved spring featuring a complient mechanism, which redirects any perpendicular

force into a lateral displacement. If the area beneath the beam is solid, compression and tensile stress within the body may only occur. If the area beneath the beam is solid, compression and only tensile stress occurs within the body.

The fact that both structures deflect laterally proves to be advantageous for the integration of the sensor with the optoelectronic components. A single LED and photodetector placed in parallel to the mass might be sufficient for measuring the modulated light flux. This integration step strongly depends on minaturisation of the 3D printed structures and, hence, on the resolution and accuracy of the printing technology per se.

2.2 Harmonic Oscillator

MEMS (micro-electromechanical systems) and NEMS (nano-electromechanical systems) resonators find their applications in the detection of chemical and biological substances, characterisation of rheological properties of fluids and energy harvesting [16]. Further, the demand of magnetometers for navigation has significantly increased, which can be seen in today's portable devices. Even though, these sensors differ with respect to their geometric layout, material properties or fabrication techniques, resonators perform their operating principle in 'resonance'. In detail, interaction with the environment influence the sensor's resonant behavior in form of a frequency shift or the change of height and sharpness of the resonant peak. To obtain the maximum output signal, resonant MEMS sensors are externally actuated to enforce oscillation near the eigenfrequency ω_0. Hence, interferences besides the resonance $\omega \neq \omega_0$ are suppressed and the signal of interest with $\omega \approx \omega_0$ is amplified. This contributes to an increased signal-to-noise ratio (SNR). The mechanical motion of such a structure can be detected either electronically, e.g. with a piezoresistive readout or optically by, e.g. laser deflection or the change of light flux detected by a photodetector. For small deflections of the cantilever relating to the initial position elastic material behavior can be considered and is assumed for the aforementioned 3D printed structures. Here, Hooke's law is valid and the system's oscillation can be described with the theory of a simple damped driven spring-mass system [17].

2.2.1 Simple Harmonic Oscillator

A simple harmonic oscillator consists of a mass m attached to a spring with stiffness k. If the mass is displaced from the equilibrium position, a restoring elastic force tends to regain the systems initial position. With Newton's second law of motion, the equation of motion of this system can be written as

$$\begin{aligned} F = m\,a = m\,\ddot{x} = -kx, \\ \text{or} \quad \ddot{x} + \omega_0^2 x = 0, \end{aligned} \tag{2.1}$$

where $\omega_0 = \sqrt{k/m}$ is the oscillator's angular eigenfrequency. The solution of this simple differential equation can be given in the form of a linear combination of sine and cosine functions which is alternatively expressed as

$$x(t) = C\,\sin(\omega t + \phi) \tag{2.2}$$

where C is the amplitude and ϕ the phase of the oscillation. At initial time $t = 0$, the amplitude and phase are given by

$$C = \sqrt{\frac{v_0^2}{\omega^2} + x_0^2} \quad \text{and} \quad \phi = \arctan\left(\frac{x_0\omega_0}{v_0}\right), \tag{2.3}$$

with the velocity v_0.
The total energy of a simple harmonic oscillator stays constant at all time and is characterised by a continual back and forth flow of kinetic and potential energy.

$$E_{\text{tot}} = \frac{1}{2}m\dot{x}^2 + \frac{1}{2}kx^2 = \frac{1}{2}mC^2\omega_0^2 = \text{const.} \tag{2.4}$$

2.2.2 Damped Harmonic Oscillator

So far, friction has been neglected ($E_{\text{tot}} = \text{const.}$) which is now introduced at the damped harmonic oscillator. Friction as force which opposes motion is assumed to be proportional to velocity $F_f = -c\dot{x}$ where c is the viscous damping coefficient which is part of the damping constant $\gamma = c/(2m)$. It damps the vibration and dissipates the energy E_{tot} in the form of heat. The corresponding equation of motion reads

$$\begin{aligned} F = m\,\ddot{x}\,(t) = -c\dot{x}\,(t) - kx\,(t)\,, \\ \text{or,} \quad \ddot{x}\,(t) + \frac{c}{m}\dot{x}\,(t) + \omega_0^2 x\,(t) = 0. \end{aligned} \tag{2.5}$$

To solve the linear differential equation, an exponential solution $x(t) = C\,\mathrm{e}^{\lambda t}$ is assumed where the roots of the characteristic polynomials are

$$\lambda_{1,2} = -\gamma \pm \sqrt{\gamma^2 - \omega_0^2}\ . \tag{2.6}$$

Thus, the general solution is given as

$$x(t) = \mathrm{e}^{-\zeta\omega_0 t}\left(C_1 \mathrm{e}^{\omega_0\sqrt{\zeta^2-1}\,t} + C_2 \mathrm{e}^{-\omega_0\sqrt{\zeta^2-1}\,t}\right) \tag{2.7}$$

with the dimensionless damping factor $\zeta = \gamma/\omega_0$. The factor $\mathrm{e}^{-\zeta\omega_0 t}$ causes an exponential decay of the amplitude in the damped oscillating system. There are three cases how the damped harmonic oscillator behaves according to the value of the expression $\sqrt{\zeta^2 - 1}$. If $\zeta = 0$ no damping occurs and Eq. (2.5) reduces to the Eq. (2.2) of the simple harmonic oscillator.

Case I Underdamping. For small damping factors $\zeta < 1$, Eq. (2.7) becomes

$$x(t) = C\,\mathrm{e}^{-\zeta\omega_0 t}\cos\left(\omega t + \phi\right). \tag{2.8}$$

Here the system oscillates with a slightly lower frequency $\omega = \omega_0\sqrt{1-\zeta^2}$ than the undamped case (see Fig. (3b), $\zeta = 0, 0.3$). This frequency shift is almost negligible, e.g. if ζ is set large enough so that ω differs notable from ω_0 the oscillators amplitude will vanish after a few cycles. For $\omega = 0.4\,\omega_0$, the amplitude of Eq. (2.8) will decrease after one cycle ($\omega t = 2\pi$) to

$$C\,\mathrm{e}^{-(\zeta/0.4)\omega t} = C\,\mathrm{e}^{-\left(\sqrt{1-0.4^2}/0.4\right)\omega t} = C\,55.93\times 10^{-6}\ .$$

Case II Overdamping. If $\zeta > 1$, the general solution can be expressed with hyperbolic functions, considering the initial conditions $x(0) = x_0$ and $\dot{x}(0) = 0$.

$$x(t) = \frac{x_0}{\omega}\mathrm{e}^{-\zeta\omega_0 t}\left[\omega\,\cosh\left(\omega t\right) + \zeta\omega_0\,\sinh\left(\omega t\right)\right] \tag{2.9}$$

The amplitude decays exponential without oscillation at a faster rate than the critically damped oscillator (compare $\zeta = 1, 3$ in Fig. (3b)).

Case III Critical Damping. The ansatz function has to be expanded to $x(t) = C\,t\,\mathrm{e}^{\lambda t}$ to obtain two independent solutions in the case of critical damping ($\zeta = 1$). No oscillation occurs and the oscillator returns to the steady state position in one period (Fig. (3b)). Considering the initial conditions, the solution becomes

$$x(t) = x_0\left(1 + \omega_0 t\right)\,\mathrm{e}^{-\omega_0 t}. \tag{2.10}$$

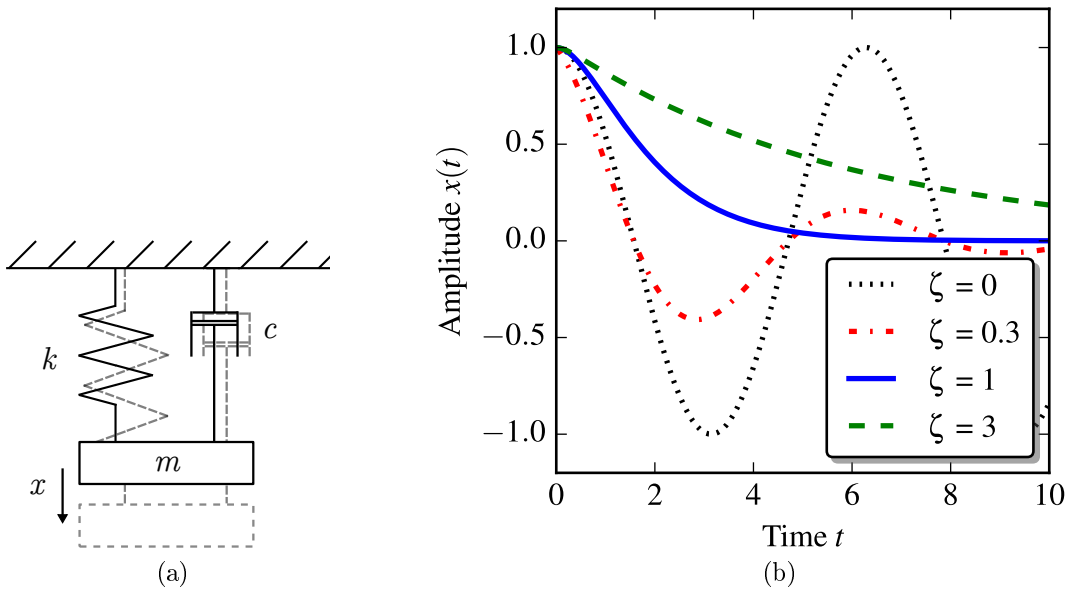

Figure 3: (a) schematic of the damped harmonic oscillator and oscillator displacements for different damping factors considering the initial conditions $x(t=0) = x_0$ and $\dot{x}(t=0) = 0$ (b).

2.2.3 Driven Damped Harmonic Oscillator

To compensate energy dissipation, the harmonic oscillator can be externally excited with a driving force $F_\mathrm{d} \mathrm{e}^{\mathrm{i}\omega t}$. The corresponding equation of motion reads

$$\ddot{x}(t) + 2\omega_0 \zeta \dot{x}(t) + \omega_0^2 x(t) = \frac{F_\mathrm{d}}{m} \mathrm{e}^{\mathrm{i}\omega t} \ . \tag{2.11}$$

This can be rewritten for the complex amplitude C with the ansatz solution $x(t) = C\,\mathrm{e}^{\mathrm{i}\omega t}$ as

$$C = \frac{F_\mathrm{d}}{m\,(\omega_0^2 - \omega^2 + \mathrm{i}2\zeta\omega\omega_0)} \ . \tag{2.12}$$

Taking the absolute value of Eq. (2.12) to extract an actual physical quantity, results in the amplitude

$$A := \sqrt{C \cdot C^*} = \frac{F_\mathrm{d}}{m\sqrt{\left(\omega_0^2 - \omega^2\right)^2 + \left(2\zeta\omega\omega_0\right)^2}} \ , \tag{2.13}$$

with the associated phase angle

$$\tan\phi = \frac{\mathrm{Im}\,(C)}{\mathrm{Re}\,(C)} = \frac{-2\zeta\omega\omega_0}{\omega_0^2 - \omega^2}. \tag{2.14}$$

It must be mentioned that the maximum amplitude does not occur exactly at the oscillator's angular eigenfrequency, but is slightly shifted by the damping factor. This resonance is given as

$$\omega_\mathrm{R} = \omega_0\sqrt{1-2\zeta^2}. \tag{2.15}$$

The frequency response and the denoted frequency shift of the maximum amplitude are shown in Fig. 4.

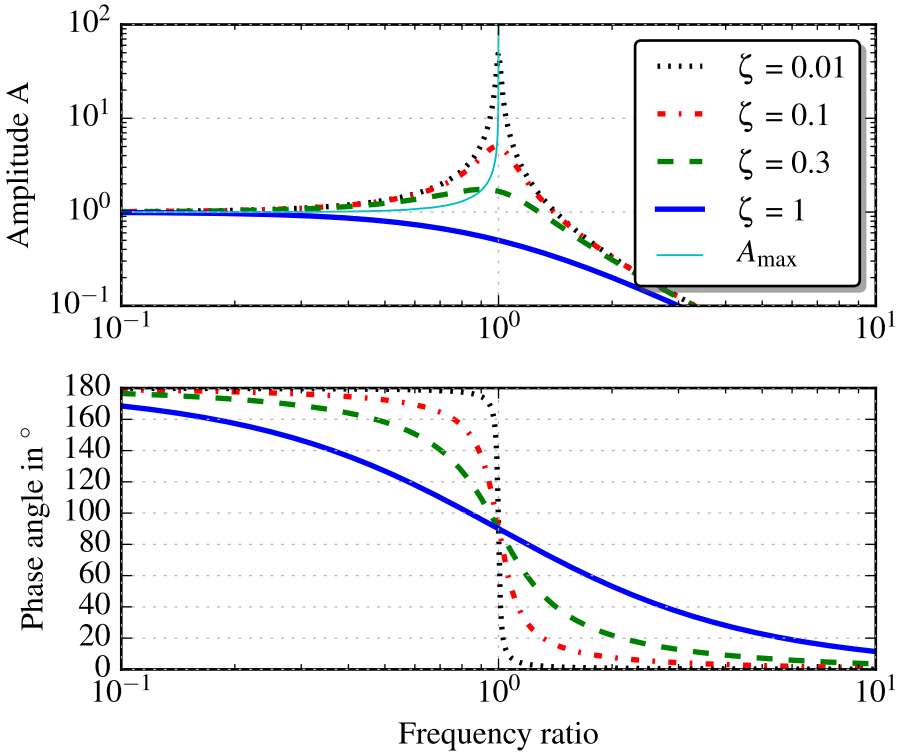

Figure 4: Amplitude and phase angle of the driven damped harmonic oscillator for different damping factors. The curve for A_max illustrates the maximum amplitude for different damping factors.

2.3 Quality Factor

In literature, the quality factor Q is commonly used instead of the damping factor ζ. It is a dimensionless number which denotes the number of oscillations it takes until the amplitude decreases to a certain value in transient solutions and indicates energy dissipation relative to the stored energy of the oscillator's steady state vibration:

$$Q = 2\pi \frac{U_{\max}}{W_{\mathrm{K}}} \approx \frac{1}{2\zeta} \tag{2.16}$$

where $U_{\max} = \frac{1}{2}kx^2$ is the maximum elastic energy stored in the spring and $W_{\mathrm{K}} = \int_0^{2\pi/\omega} F_{\mathrm{d}} \mathrm{e}^{\mathrm{i}\omega t} \dot{x}\, \mathrm{d}t$ is the energy loss per cycle at resonance ω_0.
The $-3\,\mathrm{dB}$ *bandwidth method* is commonly used to obtain Q in the vicinity of the resonant peak. From a measured response amplitude, the natural frequency ω_0 and the frequency bandwidth $\Delta\omega$ (corresponding to a response value of $A_{\max}/\sqrt{2}$) can be extracted to estimate the quality factor as

$$Q = \frac{\omega_0}{\Delta\omega}\,. \tag{2.17}$$

This approximation is appropriate for resonators with small damping. An example in [16] shows that the Q value extracted from a response amplitude with the $-3\,\mathrm{dB}$ *bandwidth method* differs 2 % only when compared with the analytical solution for an oscillator with an actual quality factor of 5. Equation (2.17) also states the necessity for a trade-off between the bandwidth and quality factor.

Various Damping Mechanisms
The energy loss of a resonator embodies many different mechanisms which contribute individually to the total quality factor. They can be summed up to a total value as

$$\frac{1}{Q_{\mathrm{total}}} = \sum_i \frac{1}{Q_i}\,. \tag{2.18}$$

Mentionable damping mechanisms are air damping, surface damping, damping through anchors, electrical damping, thermoelastic damping (TED) and damping through phonon scattering i.e. the Akhiezer effect.
Due to the operation principle of the proposed structures at atmospheric pressure, viscous damping might be the most pronounced damping mechanisms caused by the movement of the oscillating mass in precense of air. Further, intrinsic material damping shall be considered as well. Polymers show a viscoelastic behaviour, i.e. energy is lost during oscillation caused from the partly viscous material behavior. Therefore, the initial form of a previously deformed viscoelastic structure cannot be fully restored [18].

2.4 Lorentz Force Actuation

Lorentz force sensors are based on a elastic mechanical structure which interacts with external magnetic fields. Hence, a moveable mass (e.g. double-clamped cantilever) contains a current (**I**) conducting layer that sense a force when placed in an external magnetic field **B**. This generated Lorentz force $\mathbf{F}_\mathrm{L}$ acts as load on the mass's surface and deflects the structure. The resulting force on a current carrying conductor with the length l in a magnetic field is given as

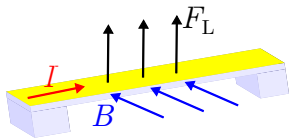

Figure 5: Schematic of the Lorentz force $\mathbf{F}_\mathrm{L}$ acting on a current **I** carrying clamped-clamped cantilever in the presence of a magnetic field **B**.

$$\mathbf{F}_\mathrm{L} = l\,(\mathbf{I} \times \mathbf{B})\,. \tag{2.19}$$

A schematic of Lorentz force actuation is illustrated in Fig. 5 [19].

2.5 Sensitivity S

The sensor sensitivity is extensively used in literature for comparison purpose, despite of the sensor's differences in fabrication techniques, excitation principle or read out mechanisms. The sensitivity for a magnetic field sensor is expressed by the ratio of the change of the output voltage which arises by a change of the external field

$$S = \frac{\partial V_\mathrm{out}}{\partial B}\,. \tag{2.20}$$

Depending on the sensor's operating principle, the sensitivity can be extended into a product of several independent sensitivities. For the proposed Lorentz force magnetometers with optical readout, the sensitivity can be represented by the voltage-to-displacement sensitivity S_x and mechanical field displacement sensitivity S_B as $S = S_\mathrm{x} S_\mathrm{B}$.

Combining Eq. (2.13) and Eq. (2.19) yields the mechanical field displacement sensitivity

$$S_\mathrm{B} = \frac{\partial A}{\partial B} = \frac{Il}{m2\zeta\omega_0^2} = \frac{IlQ}{m\omega_0^2} \tag{2.21}$$

as a result of the applied harmonic force on the deflectable mass at resonance. It is evident that the sensitivity is most affected by the damping factor ζ or, equivalently, by the quality factor Q. Furthermore, the sensitivity is maximised by increasing the sensor's length l and the exitation current I along the structure's conductive lead. These improvements are limited by spatial restrictions and increased power dissipation in form of Joule's heat which may change dimensions, prestresses or even damage the structures.

The voltage-to-displacement sensitivity S_x consists of several parts which are derived as follows: S_x depends on the relative movement of the two stencil masks and therefore, on the effective open area A_eff of the apertures, through which the light flux is transmitted and subsequently detected by a photodiode. The generated photocurrent from a photodetector is expressed as

$$i_\mathrm{ph} = R_\mathrm{S} P_\mathrm{in} \tag{2.22}$$

where R_S is the detector's responsivity and P_in the incident light power[1].

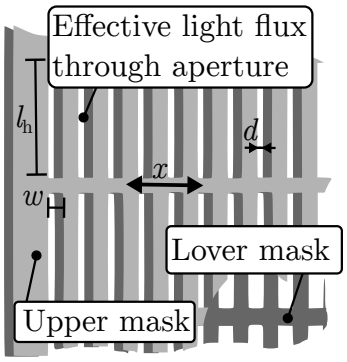

Figure 6: Schematic of the effective area where light can pass through. The upper mask's direction of oscillation is indicated with x.

The total light flux and therefore the light power depends on the effective open area of the apertures A_eff (Fig. 6)

$$P_\mathrm{in} = T_\mathrm{trans} E_\mathrm{e} A_\mathrm{eff} \tag{2.23}$$

$$\text{with } A_\mathrm{eff} = N l_\mathrm{h} d$$

where T_trans is the transmission coefficient, E_e the irradiance, N the total number of holes and $l_\mathrm{h} d$ the area of the opening. This simplified approach assumes collminated light. A transimpediance amplifier finally converts the photocurrent into the ouput voltage U_out with

$$U_\mathrm{out} = -R_\mathrm{f} i_\mathrm{ph} \tag{2.24}$$

[1] In photometry it is stated as luminous power [flux] Φ_L in unit lumen. Photometry is the science of measuring visible light based on a statistical model of the human visual response to light, i.e. visible light that is weighted according to the sensitivity of the human eye [20]. Some literatures use this notation rather than the radient flux Φ_R (or P_in for photodetectors as stated in Eq. (2.22)) in unit W.

where R_f is the amplifier's feedback resistor. The working principle of the optoelectronics and the amplifier is discussed in more detail in Section 3.
Compiling Eqs. (2.22) - (2.24), the sensitivity with respect to the relative displacement becomes [21]

$$|S_\mathrm{x}| = \left|\frac{\partial U_\mathrm{out}}{\partial x}\right| \approx R_\mathrm{f} R_\mathrm{S} T_\mathrm{trans} E_\mathrm{e} N l_\mathrm{h} \ . \tag{2.25}$$

Here, the displacement sensitivity can be improved by increasing the amplifier's feedback resistor R_f, selecting a photodetector with high responsivity R_S, raising the number of apertures N and increasing their lengths l_h. Nevertheless, an increased feedback resistance also contributes to the amplifier's equivalent input voltage noise and offset voltage, especially when R_f is higher than the photodetector's shunt resistance (see Section 3). The responsivity mainly depends on the detector's quantum efficiency η, which is enhanced by selecting semiconductor materials like InGaAs for the PD and a matching LED. The number of apertures and their length is restricted by spatial limits, in particular the mass's area A_m. Furthermore, it depends on the aperture width, e.g. a small width increases the number of apertures but may also lead to pronounced diffraction effects (see Subsection 4.1.4). On the other hand, too small chosen aperture width may also be seen at the output voltage in form of clipping effects, i.e. the mass's maximum displacement may exceed the aperture width, yielding output signals with higher frequencies.

2.6 Thermomechanical Noise

Micromechanical structures experience a force F_n in unit $\mathrm{N}/\sqrt{\mathrm{Hz}}$ caused by collision from ambient gas particles [22], which can be written as

$$F_\mathrm{n} = \sqrt{4 k_\mathrm{B} T\, c} \tag{2.26}$$

where k_B is the Boltzmann constant, T the absolute temperature and c the damping coefficient. Multiplying Eq. (2.26) with the root of bandwidth BW yields the noise equivalent force. The introduced bandwidth usually depends on the measurement setup and balances the measurement time against the level of a desired signal to the level of background noise. The presence of noise in driven damped beams concerning a finite ζ and T, is stated by the fluctuation - dissipation theorem. This thermomechanical noise is known as Brownian motion and contributes to a sensor's noise equivalent deflection

$$A_{\mathrm{n}} = \frac{\sqrt{4k_{\mathrm{B}}Tm2\zeta\omega_0 BW}}{m\sqrt{\left(\omega_0^2-\omega^2\right)^2+\left(2\zeta\omega\omega_0\right)^2}} \tag{2.27}$$

by inserting Eqs. (2.26) into (2.13) expressed for the damping factor ζ. Neglecting this noise, the mass deflection in the presence of a magnetic field B is described analogously by

$$A = \frac{ilB}{m\sqrt{\left(\omega_0^2-\omega^2\right)^2+\left(2\zeta\omega\omega_0\right)^2}}\,. \tag{2.28}$$

The dimensionless signal-to-noise ratio (SNR) is derived from the aforementioned equations to

$$SNR_{\mathrm{mech}} = \frac{A}{A_{\mathrm{n}}} = \frac{ilB}{\sqrt{4k_{\mathrm{B}}Tm2\zeta\omega_0 BW}}\,. \tag{2.29}$$

If the sensor is driven at resonance ω_0 by applying a sinusoidal current $i = i_0 \sin(\omega_0 \mathrm{t})$, the (thermomechanical) SNR becomes

$$SNR_{\mathrm{mech},\Delta\omega} = \frac{ilB}{\sqrt{4k_{\mathrm{B}}Tm2\zeta\omega_0\Delta\omega}} = \frac{ilB}{4\zeta\sqrt{k_{\mathrm{B}}Tk}} \tag{2.30}$$

where $\Delta\omega = BW = 2\omega_0\zeta$ is the resonator's bandwidth and k the spring constant. The resonator's bandwidth was estimated with the $-3\,\mathrm{dB}$ *bandwidth method* as in Eq. (2.17). Figure 7 depicts the signal and noise amplitude for the particular case of Eq. (2.30) and also indicates the dependency of the SNR on the different bandwidth. Furthermore, the minimum measurable field of Eq. (2.29) is defined by setting $SNR = 1$, which means that the signal and noise amplitude are equal and reads

$$B_{\mathrm{min}} = \frac{\sqrt{4k_{\mathrm{B}}Tm2\zeta\omega_0 BW}}{il}\,. \tag{2.31}$$

In this case, reducing the damping factor, e.g. by operating the resonator in vaccum, decreases the minimum detectable field.

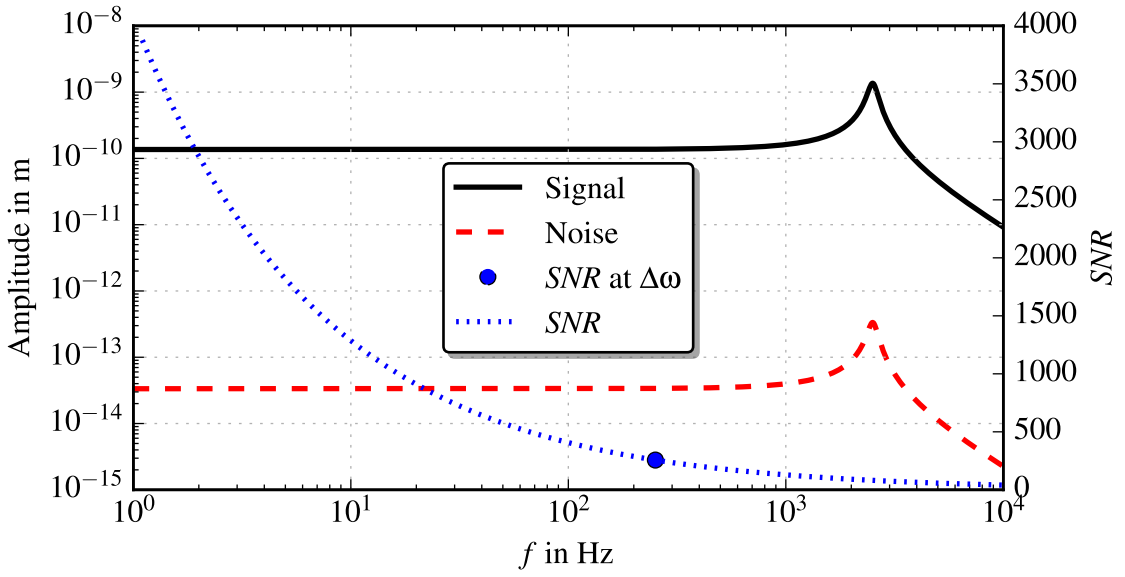

Figure 7: Output signal and mechanical thermal noise plot of a damped resonator with natural frequency $f_0 = 400\,\mathrm{Hz}$ and damping factor $\zeta = 0.05$. The sensor's noise equivalent deflection is plottet by assuming a bandwidth of $\Delta\omega = 2\omega_0\zeta$, resultant an SNR of 256. The signal-to-noise ratio is enhanced by reducing the measurement bandwidth, though increasing the measurement time.

3 Optoelectronics and Amplifier

The modulated light flux is converted into an electrical current by a photodiode and transferred into a voltage by a transimpediance operational amplifier (TIA). The readout circuit also provides the possibilty to adjust the emitting light power and perform offset compensation to suppress the steady component of the light flux, which occurs due to the initial offset between the two masks. Without compensation, the light flux will contribute to a DC component of the photocurrent which contains no valuable information and may drive the circuit into saturation.

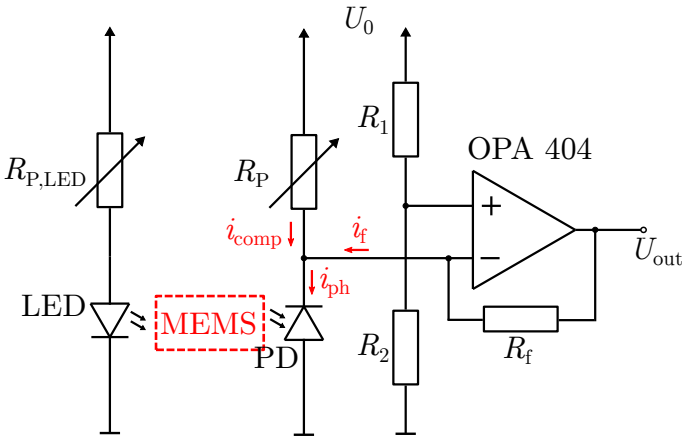

Figure 8: Schematic of the readout circuit. The transimpedance resisitor R_{f} converts the photocurrent into a voltage U_{out}. The resistors R_1 and R_2 set the bias voltage for the photodiode, whereas the potentiometer R_{p} adjusts the offset current caused by scattered light and the initial offset between the two masks.

3.1 Photodetector

A highly sensitive PIN photodiode (TEMD5110X01, Vishay Semiconductors) has been chosen because of its large area of 7.5 mm^2 and integrated daylight blocking filter. The relatively large area of the moving mass and, therefore, the effective light flux, favoured a large area photodiode. Further, a large area enables more space for the quantity of apertures, hence, increases the voltage-to-displacement sensitivity S_{x} as derived in Eq. (2.25). The daylight blocking filter suppresses the diode's sensitivity for visible light and matches the diode for 790 to 1050 nm emitters. Hence, an infrared LED with $\lambda_{\mathrm{peak}} = 880\,\mathrm{nm}$ (SFH 4680, OSRAM) is used.
The quantum efficiency and spectral responsitivity are characteristic values of a photodetector and often stated in its data sheet. The responsitivity is stated as

$$R_{\mathrm{S}} = \frac{\eta e}{h\nu} \tag{3.1}$$

where η is the quantum efficiency, e the electron charge and $h\nu$ the photon energy. A classic silicon photodiode can be pictured in an equivalent circuit consisting of a junction capacitance, a shunt resistance and a current source, all connected in parallel. This bulk resistivity is usually very high ($\sim 100\,\mathrm{M\Omega}$) and corresponds to the diode's dark current which is a major contributor to the circuit's noise [23]. The photodiode can be operated either in photovoltaic or photconductive mode. The latter has been chosen due to existing equipment, experience and the circuit's well known behaviour [24].

3.2 Readout Circuit

A schematic of the circuit is depicted in Fig. 8. The photocurrent i_{ph}, consisting of a DC component with no valuable information and an AC component is transformed into a voltage and is amplified via the TIA with feedback resistor R_{f} to $U_{\mathrm{out}} = -R_{\mathrm{f}} i_{\mathrm{f}} + U_{-}$, where U_{-} is the bias voltage. This bias is necessary to operate the photodiode in photoconductive mode, set at the OPA's inverting input pin by the resistor R_1, R_2 to $U_{-} = U_{+} = U_0 R_2 / (R_1 + R_2)$.
Alignment difficulties of the masks (discussed in Subsection 4.1.4) introduces an offset light flux, hence contributing as major component to an offset current. The offset current is compensated by the potentiometer with $i_{\mathrm{comp.}} = (U_0 - U_{+})/R_{\mathrm{P}}$, yielding an output voltage of $U_{\mathrm{out}} = -R_{\mathrm{f}}(i_{\mathrm{comp.}} - i_{\mathrm{ph}}) + U_{-}$. Other components such as temperature dependency, scattered light and imperfection from manufacturing an amplifier, i.e. mismatches and tolerances of transistor pairs, resistors, etc. also affect the TIA and contribute to input offset voltages. The final expression for U_{out} is derived by combining the aforementioned equations yielding

$$U_{\mathrm{out}} = R_{\mathrm{f}} i_{\mathrm{ph}} + U_0 \left(-\frac{R_{\mathrm{f}}}{R_{\mathrm{P}}} + \frac{R_2}{R_2 + R_1} \left(\frac{R_{\mathrm{f}}}{R_{\mathrm{P}}} \right) \right). \tag{3.2}$$

Putting the second term equal to $R_{\mathrm{f}} i_{\mathrm{DC}}$, the required value of R_{P} is computed to compensate the photocurrent's DC component. The feedback resistance was chosen to be $10\,\mathrm{M\Omega}$.
The readout circuit has potential for further improvement. By operating the photodiode in photovoltaic mode and, hence, reducing the dark current, the noise contribution can be lowered. This mode is appropiate if precision is more important than speed, which is the case for low frequency resonant MEMS [25]. However, measurements should be conducted to estimate how the the dark current affects the sensor's output signal.

4 Prototypes Fabrication and Characterisation

4.1 Manufacturing Technology

Typical MEMS processes are divided in bulk and surface micromachining. The former category is based on wet or dry etching (e.g. deep reactive ion etching, DRIE) of silicon substrates, where the latter forms structures by deposition and etching of sacrificial and structural thin films. Another method for high aspect ratio structures is the LIGA technology (German acronym for Lithographie Galvanoformung Abformung) where the photoresist is patterned with X-ray exposure followed by electroplating of a metal into the cavities left by the removed resist [26].
The aforementioned technologies require lithography processes, which actually transfer the desired information of shape onto a photoresist coated onto a (Si) substrate. Even tough trenches in substrates greater than 500 µm are feasible with the DRIE method, photo lithography is limited by its 2D spatial resolution; in other words, it is a planar process. By introducing gray-scale lithography with deep reactive ion etching, gradual shaping of height of silicon surfaces becomes possible. The photoresist may be exposed through a dot modulated chrome mask or by a direct writing process with a laser or electron beam, followed by development [27]. Hence, the silicon profile is defined by variable height of the photoresist, since silicon masked by a thicker layer is etched later compared to silicon masked by thinner resist (Fig. 9) [28].
Additionally, processed wafers might be bonded together to create complex 3D structures. Drawbacks of conventional MEMS processing are the dependency on large-scale, specialised equipment, expenses for clean room envrionments and long lead times during sequential processing of repeated use of lithography, etching and deposition [29].

4.1.1 3D Printing Technology for MEMS

As of today, multiple additive manufacturing technologies for micromachining MEMS devices are emerging, especially for small-sized manufacturing volumes and prototyping purposes. These technologies are based on inkjet deposition, laser, ion, electron beam or scanning probes to add or remove material. Rapid prototyping approaches are advantageous by compressing product development cycles, investigating different geometries and parameters that match the final designs. Limitations depend on the mechanical properties of the used materials and the achieveable resolution of 3D printing technology. Therefore, new processes to deposite materials are continuously being developed and it is visible that the minimum feature size, currently limited to 50 - 1000 µm, is further reduced [29]. This subsection shortly summarises current 3D printing technologies for micro and nano structures.

Stereolithography (SLA) is the most popular method nowadays. It works by irradiating a liquid photo-sensitive resin by a rastering laser beam to induce

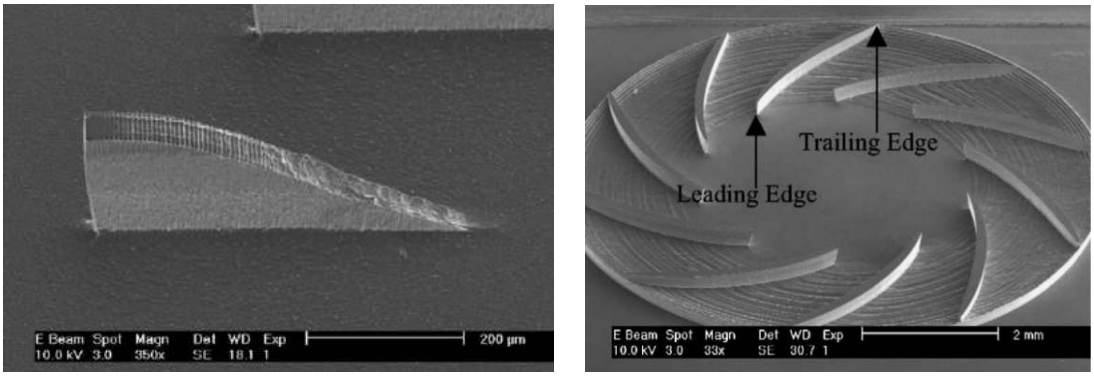

Figure 9: Test silicon wedge structure accomplished using gray-scale lithography on the left. A micro-compressor with variable height of etched silicon blades using gray-scale lithography and DRIE is depicted on the right. The bottom wall slopes from an etch depth of 400 µm at the inner radius to 200 µm at the outer radius, yielding a height of the leading edge and trailing edge to be 350 µm and 140 µm, respectively. To complete the design, another wafer would be bonded to the top of the blades for encapsulation, allowing a mass flow inlet to exit ratio of 2:1 in the vertical dimension and, thus, effectively increases compression [28].

photopolymerisation. A platform filled with the photopolymer of the desired layer thickness is scanned by a laser to transfer the model's desired shape. The platform is then lowered to the next layer filled with the polymer and again processed with the laser beam. The entire model is built by repeating these steps. After removing the excess polymer, a final curing step is performed to prevent undesireable chemical reactions that may lead to warping, cracking and dimensional instability. Minimum feature sizes of 250 - 800 µm are reported.
Better resolution is achieved with microstereolithography which is based on a similar principle. Here, the geometry is printed by a stationary focused laser beam with a precisely horizontally moving platform filled with a photoactive resin. This approach overcomes the difficulty of beam steering and focusing, but at the expense of longer fabrication times.
Flexible polyethylene-like, rigid ABS-like and polypropylene-like materials are in use. The suffix '-like' annotates a difference in the chemical nomenclature from the originial substances, hence they are modified, but still feature similar mechanical properties [29].

Multijet Modelling (MJM) or polyjet is a variant of the SLA which dispenses and cures a photoploymer through the print head simultaneously. This method offers a high layer resolution of around 16 µm, which comes close to the resolution requirements of a typical MEMS device. The most common materials are acrylate based with rigid, elastic, translucent or opaque properties. The polyjet process is extensively used in arts due to the offered "on demand" flexibility [29].

The stereolithography processes above mentioned are based on single photon polymeristaion, e.g. one photon absorption, where light may be absorbed either directly by the resin or by a photosensitiser which acts as a catalyst absorbing light, hence transferring energy to the monomer. The achievable resolution in lithography as well as in optical microscopy is proportional to the wavelength λ of the light, expressed by Abbe's diffraction limit $d = \lambda/(2\,NA)$, where NA is the numerical aperture. Hence, the spectrum of ultraviolet light to high energy ultraviolet radiation, spanning wavelenghts from 400 nm down to 10 nm, are used. The absorption rate is proportional to the light intensity compared to the squared dependency for two photon absorption in 3D direct laser writing. The equation describing the intensity attenuation is given with $\mathrm{d}I/\mathrm{d}z = -\alpha I - \beta I^2$ where α is the absorption coefficient, β is the two-photon absorption coefficient and $\mathrm{d}z$ a thickness element where power is absorbed [30, 31].

3D direct laser writing is a nonlinear optical process, typically based on a near infrared femtosecond pulsed laser that is focused to a spot within the volume of a photoresist. The threshold for initiating the polymerisation is exceeded only in the vicinity of the focus, where the intensity of the light is the highest. Complex 3D micro- and nanostructures such as photonic crystals (Fig. 10b), photonic metamaterials, pentamode mechanical metamaterials and components such as waveguides, coupler, resonators, micro lenses and 3D data storage devices can be accomplished with this technique [32, 33].

Selective laser sintering (SLS) is based on fusing small particles of a powder into a finished part. Powder is dispensed onto a platform and subsequently melted and sintered with a high-power laser. An additional thin layer of powder is added and solidified into the cross section of the structure again. This layer-by-layer process is repeated until the entire 3D structure is built. A typical powder layer thickness of 5-20 µm and micro parts with a total feature sizes ranging from several milimeters down to about 20 µm are feasible [32]. This manufacturing technique is able to process plastic powder materials like nylon and metal powder such as molybdenum, titanium and stainless steel [29]. A metal sintered micro gear wheel is depicted in Fig. 10c.

Fused deposition modelling (FDM) is capable of printing microstructures by ink extrusion through a heated micro - nozzle. Mainly thermoplastics in the form of thin filaments are processed, however, depending on the printer head, paste-like materials such as chocolate, porcelain clay or wood pulp are also possible. Previous work [34] has shown that functional inks containing $Li_4Ti_5O_{12}$ (LTO) and $LiFePO_4$ (LFP) allows of printing Li ion microbatteries (Fig. 10d).

Focused ion beam writing in combination with silicon deposition and selective etching is another approach of creating a layer by layer 3D model. Gallium (Ga) ions are implanted in a Si layer, followed by chemical vapor deposition

of a Si layer. Repeating this process defines the resulting Si structure. A final wet etch with potassium hydroxide (KOH) releases the structure. Thereby, the implanted Ga ions provide etch selectivity [35]. Silicon beams with dimensions in the order of 1 µm or even smaller are shown in Fig. 10e.

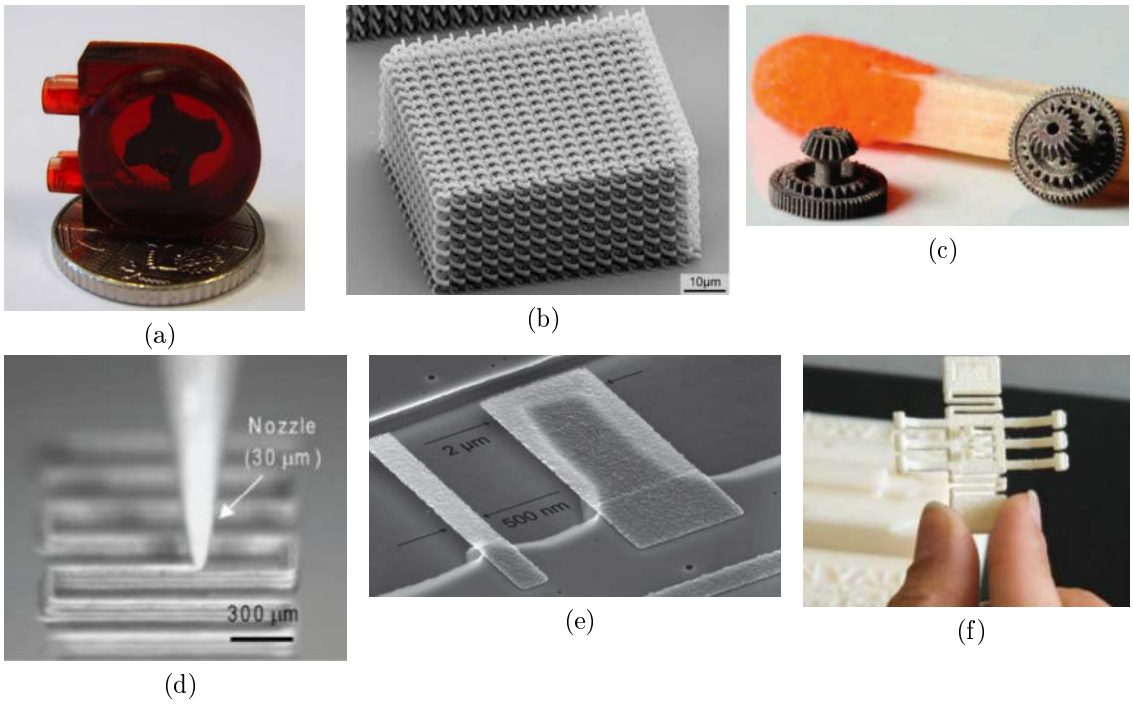

Figure 10: Exploratory objects manufactured with different 3D printing technologies. (a) shows a flow sensor printed with microstereolithography, where the resin incorporates magnetite nano particles. Applying an external magnetic field sensor, the impeller's rotation and hence the flow rate can be determined [36]. b) depicts a 3D photonic crystal fabricated using 3D direct laser writing based on two-photon polymerisation, whereas a metal sintered micro gear wheel is illustrated by Sub-Figure c) [32]. (d) $LiFePO_4$ ink deposition through a 30 µm nozzle [34]. (e) shows an SEM image of Si cantilevers fabricated with ion beam writing, where the narrow beam was etched free, while the wide beam is still supported [35]. (f) an upscaled MEMS capacitive switch model for educational purposes [37].

Low-cost 3D printing technologies for rapid prototyping are currently limited by the resolution required for MEMS fabrication. In addition, mechanical properties of polymer materials cannot compete with commonly used processing materials such as Si, Al or Ti. The tensile modulus of Si is approximately two orders of magnitude larger than the one of polycarbonates or polyacrylates.
Nevertheless, 3D printing is a useful and effective assessment tool to demonstrate working principles for designs before initiating costly conventional MEMS technology. Further, potential as an educational tool for MEMS design and fabrication

is given, where students experience the challenge of iterative modelling and design processes on upscaled models of MEMS devices (Fig. 10f)[37]. Table 2 summarises the resolution (layer thickness), the minimum feature size and applicable materials of the above mentioned 3D printing technologies. Other printing methods are discussed in [29] and [32].

4.1.2 Prototype Fabrication

The prototypes investigated within this studies are manufactured with state-of-the-art 3D printing Multijet Modeling (MJM) technology. Acrylate as print material has been chosen due to the best possible printing resolution on the market for low-cost manufacturing, its insulating characteristic and easy accessibility. Acrylate is a photo reactive resin which cures upon exposure to light. A minimum layer thickness of 16 µm is achieved in the layer-by-layer printing of the prototypes. Nevertheless, the structural design is restricted by the manufacturer to guarantee handling and cleaning of the prototypes. A minimum thickness of 0.3 mm for walls and 0.6 mm for free standing areas are recommended. Otherwise, too long and too thin free-standing structures might collapse when the wax-like support material is melted. After the printing process, the samples are cleaned in an ultrasonic bath and rinsed with water. This step is necessary to completely remove remaining wax residues which support the structure's cavities during the printing process [38, 39]. The outcome is a translucent ojbect (see Fig. 11a). Additionally, the spaces between free-standing structures must be large enough to prohibit clumping and guarantee the safe removal of the support wax. Figure 11 depicts limitations of the 3D printing process such as wax residues, small escape holes resulting in acrylic remains and surface roughness. The averaged roughness R_a measured with a Dektak 150 Profilometer is expressed with $R_\mathrm{a} = (1/n) \sum_{i}^{n} |y_i|$. Hence, the surface roughness for the out-of-plane magnetic field sensor was measured alongside an edge of 2 mm length is 12 µm as shown in Fig. 11b.

4.1.3 Surface Coating

To excite the prototype's mass with Lorentz force, the surface must be treated to become conductive.
Several coating techniques and materials were tested to achieve the best possible surface conductivity. Major problems arise in reducing the resistivity along the springs which is due to the spring's length and the relatively thin coating. The irregular surface impedes this process. Gold (Au), nickel (Ni) and silver (Ag) have been evaporated, sprayed and brushed, respectively, on the prototype's surface. Au and Au on top of copper (Cu) were evaporated with the electron beam method in vacuum. Thus a controlled thickness of the coating was achieved. A disadvantage of the spray coating approach is the difficulty to find the ideal amount of Ni to achieve a

Printing methods	**SLA**	**MJM**	**SLS**	**Direct laser writing**	**FDM**	**Ion beam writing**
Resolution (in µm)	50-150	16-50	5-100	0.1	30-250	-
Min. feature size (in µm)	250-800	500	20-1000	1-200	60-700	0.033
Materials	ABS, PE, PP, PC, acrylic resin	acrylic resin, ABS, PP,	nylon, Mo, Bronze Cr alloy, Al-Ni-alloy, Ti, stainless steel	nylon, siloxane, hydrogels,	PC, PPSF chocolate, ceramics, metals	silicon, W, Au, Al, Pt

Table 2: The resolution, feature size and the materials are compiled from [29, 32, 38, 39].

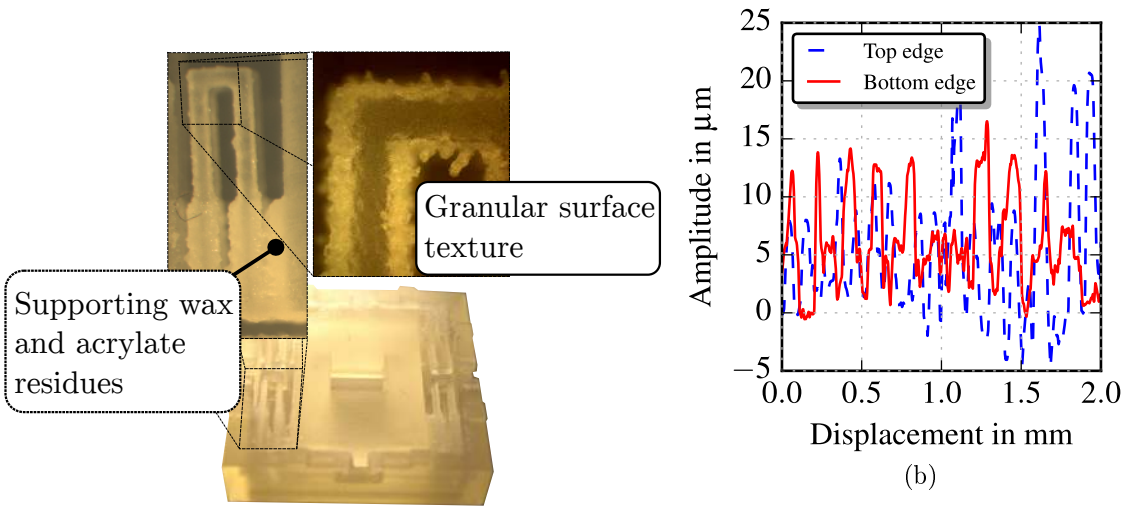

(a) (b)

Figure 11: (a) limitations of 3D printing and measurement results of the surface roughness alongside the outer frame of an in-plane magnetometer (b).

low surface resistance and provide evenly distributed Ni particles. Designed cavities on the frame interrupt the conductive coating and force the excitation current over the spring suspended mass. Figure 12 and Table 3 summarise the different surfaces and the associated resistance for the out-of-plane magnetic field sensor.
High surface conductivity is desirable to minimise heating of the springs due to the supplied current. Furthermore, the springs ought to have an identical resistance to avoid asymmetric deformation caused by Joule's heating in the beams.
The in-plane magnetic field sensor requires small and thin areas of highly conductive leads, which is achieved with the silver conductive paint. The current carrying paths are connected in series, where the resulting surface resistance is 20 Ω.

Future possible coating techniques may be based on immersion. The prototypes are dipped in liquid conductive paints with low viscosity and dried afterwards. Different coating thicknesses are feasible by repeating this process.

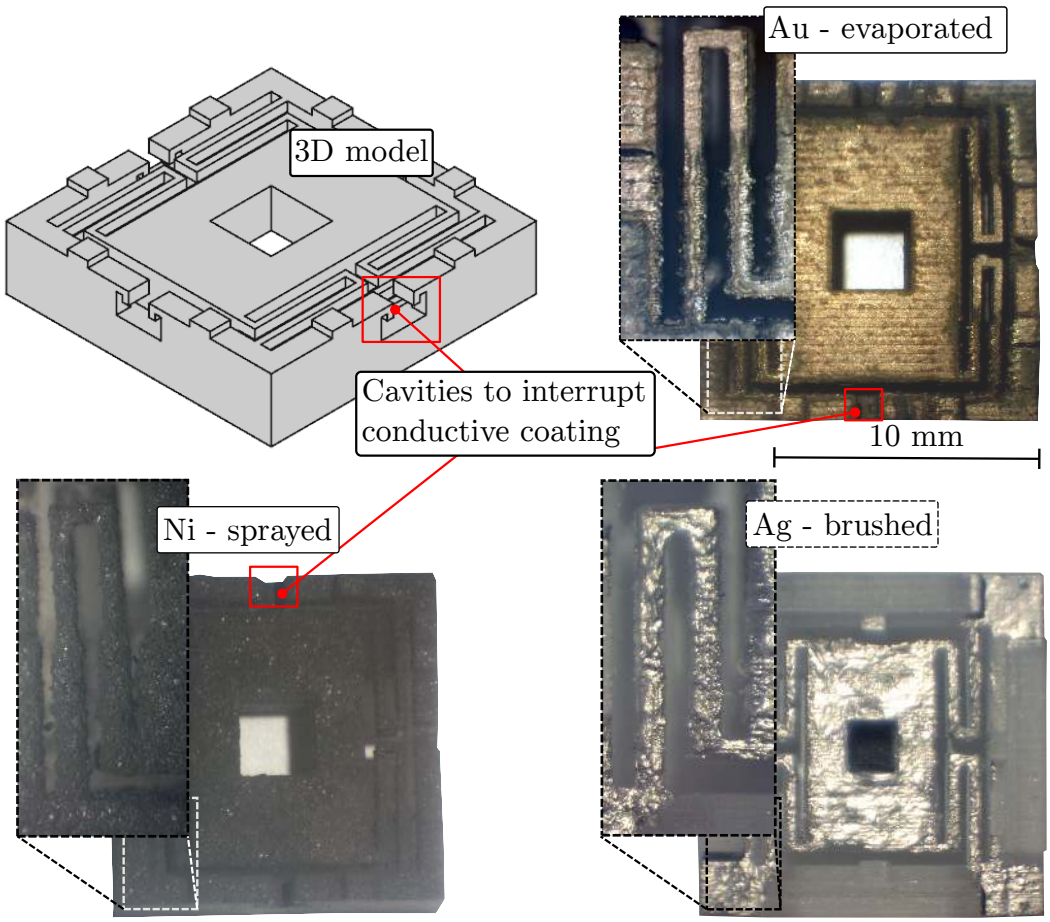

Figure 12: Different surface coating are shown for an out-of-plane magnetic field sensor. Some areas of the Au evaporated samples exhibit a darker color, which is due to the partial decomposition of the acrylic plastic.

Coatings	**Au-Cu (500 nm)**	**Au (100 nm)**	**Ni**	**Ag**	**Ni+ Ag painted springs**
moveable mass	10 Ω	-	50 Ω	2 Ω	50 Ω
springs	-	-	200 - 400 Ω	1 - 2 Ω	10-50 Ω
R_{total}	-	-	500 - 800 Ω	5 - 10 Ω	80 - 150 Ω

Table 3: Resistances of the different coatings measured with a FLUKE 179 digital multimeter. The resistance of the moveable mass was measured diagonally, from the lower left to the upper right corner for an out-of-plane magnetic field sensor. The resistances of the four springs were measured separately. They vary strongly for the Ni coated surface, which is due to the difficulty to evenly distribute Ni particles. R_{total} is the total resistance measured vertically from one edge of the outer frame to another, i.e. direction of the current flow, including the moveable mass, two springs and the connective port.

4.1.4 Glass Wafer Fabrication, Mask Alignment and Diffraction Phenomena

In order to enable light modulation, either, static and moveable apertures must be provided during the 3D print process as part of the structure or, they are manufactured seperately in form of glass wafers or foils and, thus, bonded onto structure. Previous work [14] has shown fabrication steps for chromium coated glass chips, fabricated from a 350 µm Pyrex® glass wafer which can be summarised as:

1. The geometry of the apertures are patterned by photolithography on the glass surface.

2. Cr is deposited through thermal evaporation onto the surface.

3. Removal of the photoresist (etching the sacrificial layer).

Two types of glass masks with apertures sizes of $100\times10\,\mu m^2$ and $100\times20\,\mu m^2$ were fabricated. After dicing, the glass chip's size are $4\times4\,mm^2$ and $7\times5\,mm^2$ for the deflective mass and fixed part, respectively.
Rotational misalignment may occur during the gluing process of the two glass masks which is due to creeping processes during the adhesive's hardening. Structural deflection and rough surfaces are results of the 3D printing limits and do not guarantee uniform distances between both masks. Therefore, a relativly large distance between the glass masks must be considered to avoid frictional contact. However, the relativly large distance of 300 µm between the two Cr masks impedes focalising with an optical microscope, hence increases the difficultiy of alignment. Taking the masks with the biggest aperture of $100\times10\,\mu m^2$, a rotational misalignment of $> 5°$ leads to a significantly worsened light modulation. The angle of allowed misalignment decreases for smaller apertures.
Figure 13 depicts this rotational misalignment and shows FEM simulation results for the effective light flux through both apertures in dependence of mask rotation and displacement. The simulation results in Fig. 13b show that the linear domain, where a linear change of light flux is expected, decreases for rotational misaligned masks and turns into a sinusoidal-like and sinusoidal change of light flux for rotation$<5°$ and rotation$>5°$, respectively.

Due to the large distances between both glass masks, light diffusivity is increased and reduces the ability of light modulation.
To reduce the diffraction phenomena, the aperture width can be enlarged. Diffraction is described by Huygen's principle, which is the bending of waves as they pass through an aperture. The bending vastly depends on the aperture width d and is expressed by $\sin\theta = \lambda/\mathrm{d}$ for the first order diffraction. FEM simulation results for different aperture widths are depicted in Fig. 14. According to the results, masks with slit widths of > 50 µm are recommended.

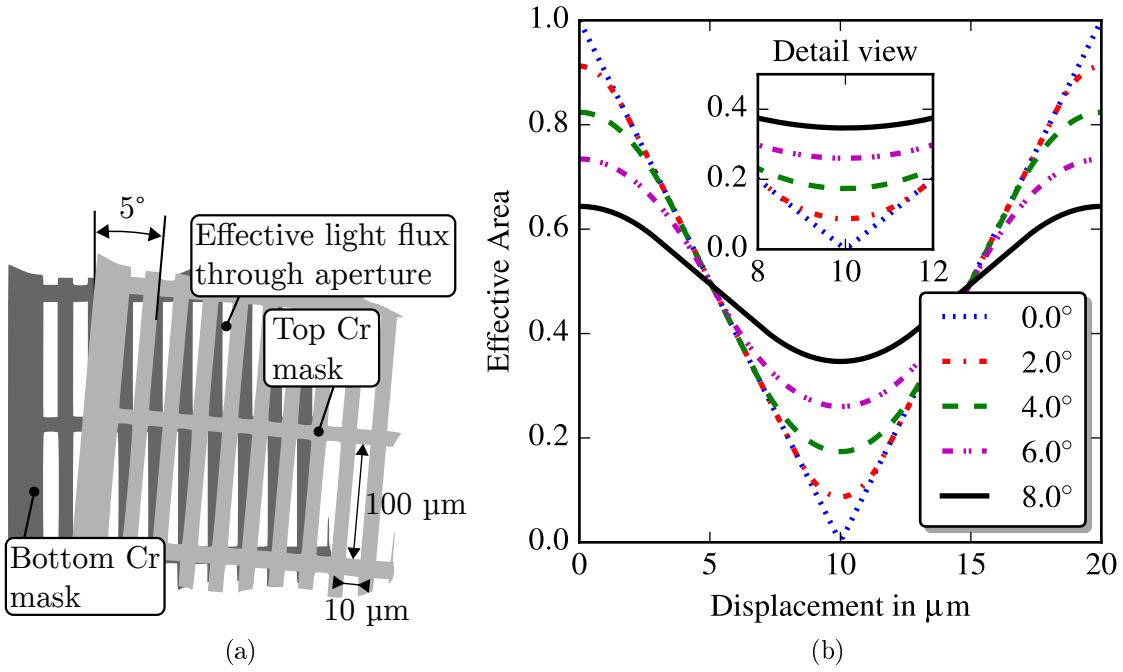

Figure 13: Schematic of misaligned apertures (a). The resulting light flux through both chromium mask depending on the rotational misalignment is depicted in (b). The plots are the results from FEM simulation. A single slit of $10 \times 100\,\mu m^2$ was displaced over a fixed aperture, thus calculating the residual free area to yield the effective area. At 10 µm displacement, the slit fully covers the free area when no rotational misalignement occurs. The inset clearly depicts a decrease in changeability of the effective area, hence light flux through the apertures, when the upper mask is rotated and not operated in the linear domain. Compared to the ideal case, the area changes only to 60 %, 30 %, 20 % and 15 % for 2°, 4°, 6° and 8° rotation, respectively, for a displacement range depicted in the inset.

4.2 FEM Analysis

Finite element method (FEM) simulations are very well suited to investigate MEMS layouts, especially for complex springs and structural designs. The scientific software COMSOL Multiphysics® has been used to determine the structure's eigenfrequency and behaviour in the presence of a magnetic flux density. To obtain accurate solutions in reasonable time, the mesh size must be chosen adequately, e.g. mesh refinement is necessary for small domains like springs and can be set coarse at large and stiffer areas. Figure 15 depicts the out-of-plane magnetic field sensor with mesh refinement at flexural areas.

The finite element method for structural mechanics is based on a discrete-coordinate

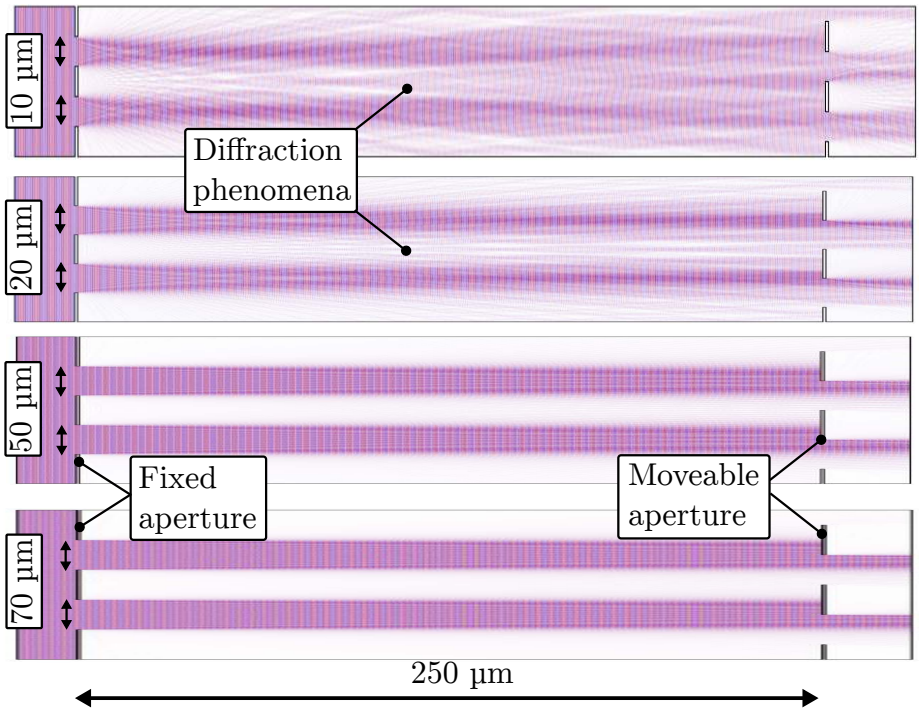

Figure 14: FEM simulation results for the light diffraction phenomena for different slit widths. An incident plane wave with a wavelength of 800 nm passes through static apertures. Light diffraction is simulated for 250 µm distance between both apertures and modelled with perfectly absorbing boundaries. The increased light diffusivity for large distances between the fixed and moveable aperture results in decreased information from light modulation, especially for small aperture widths.

approach with lumped mass. Hence, inertia and stiffness are uncoupled, where massive areas are assumed to be rigid and highly flexible parts are assumed massless [16].

Different FEM simulations have been performed within this thesis. They can be summarised as follows: The former Subsection 4.1.4 discussed simulation results of light propagation through Cr glass masks to demonstrate diffraction patterns and the problem of light diffusivity when the apertures are aligned at a large distance. Further, a geometry sweep simulation illustrates the effect of rotational misaligned apertures. The results of the prototypes' natural frequencies are shown in Subsection 4.4 and 4.5. In addition to the eigenfrequency analysis, simulations of the in-plane magnetic field sensor's behavior in a perfect environment has been conducted to investigate the mass's deflection in more detail (see Subsection 4.5.2). The first simulation assumes an ideal orientated magnetic flux density whereas the second simulation shows an external inhomogenous magnetic field distribution. Damping was set arbitrarily by COMSOL.

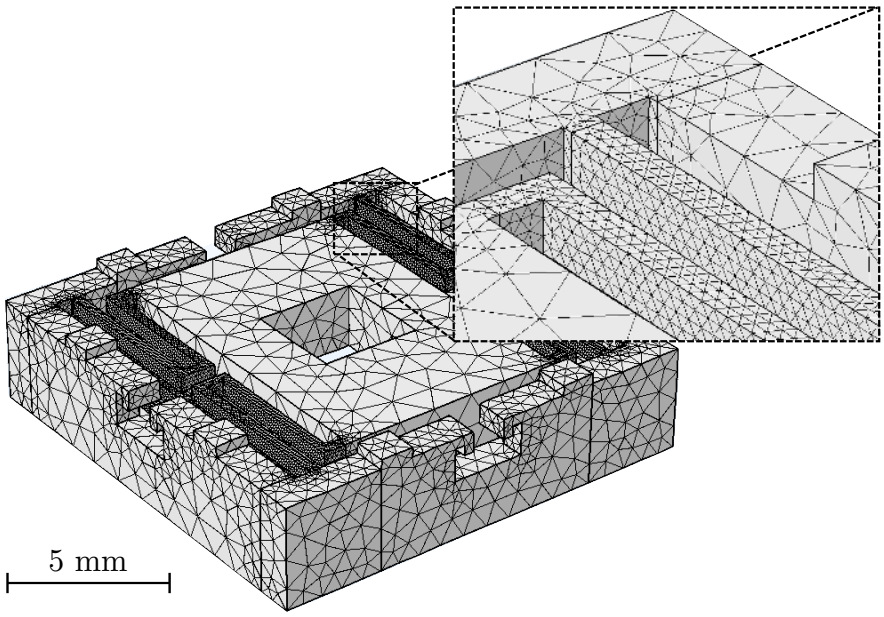

Figure 15: Mesh of a 3D geometry with tetrahedral elements. The maximum element size of the coarser and finer areas are limited to 1.5 mm and 150 µm, respectively.

4.3 Measurement Settings

The experimental setting for the characterisation of the magnetometers is depicted in Fig. 16a. The sensor mounting and transimpediance amplifier circuit are attached onto a breadboard made of aluminium with vibration absorbing Sorbothane feet [40] and shielded with a grounded metal housing to avoid scattered light and electromagnetic coupling from the surrounding. The measurement is controlled via a Raspberry Pi and fully automated to guarantee reproducibility. Measurement programs and evaluation scripts were coded in Python to control instruments such as the current source (Keithley 6221 AC and DC current source) and lock-in amplifier (SR830). A oscilloscope is used for monitoring the output signal during offset compensation.

A more detailed representation of the custom made mounting device is depicted in Fig. 16b. It is designed for both the out-of-plane and in-plane magnetic field sensors. The excitation current is applied via spring probe pins, which also clamp the sample into the cavity. The mounting device is also designed with spaces for permanent magnets to ensure a reproducible magnetic field and easy exchange of magnets. Slots for disc magnets are on the top and bottom part of the mounting device (Fig. 20a), whereas cavities for pole shanks, connected with rectangular magnets are located sideways to the sensor inlet (Fig. 30a). The disk magnets shall produce a vertical magnetic field to characterise the out-of-plane magnetic field sensor, whereas a 'pseudo' horizontal magnetic field shall be established between these poles.

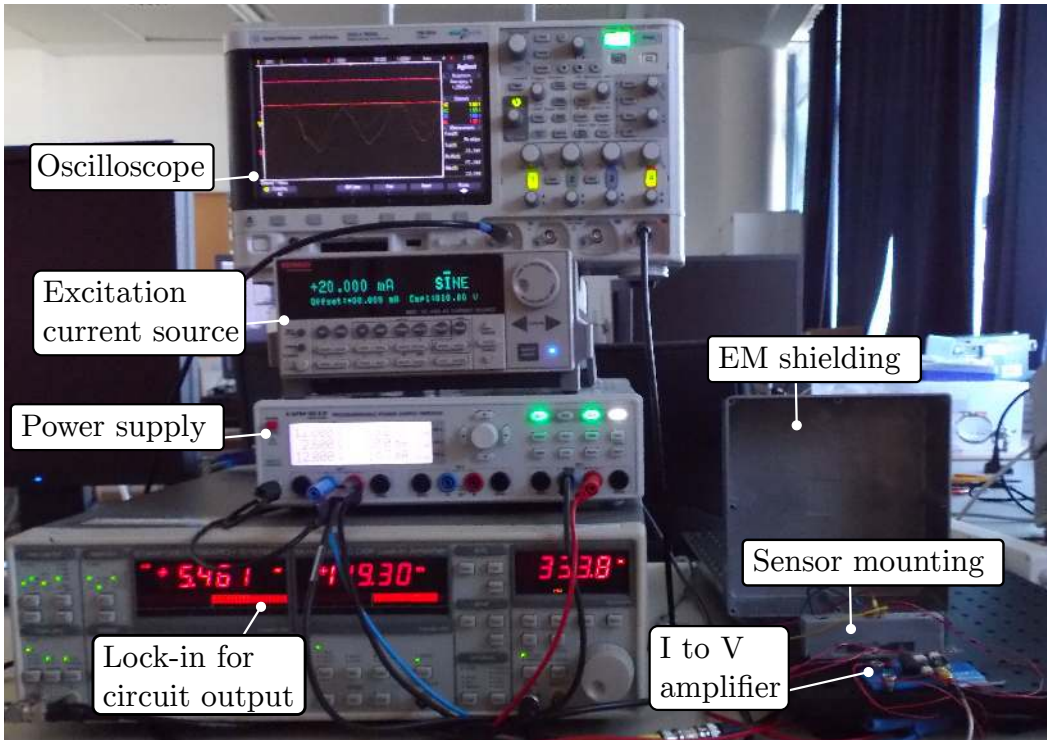

(a)

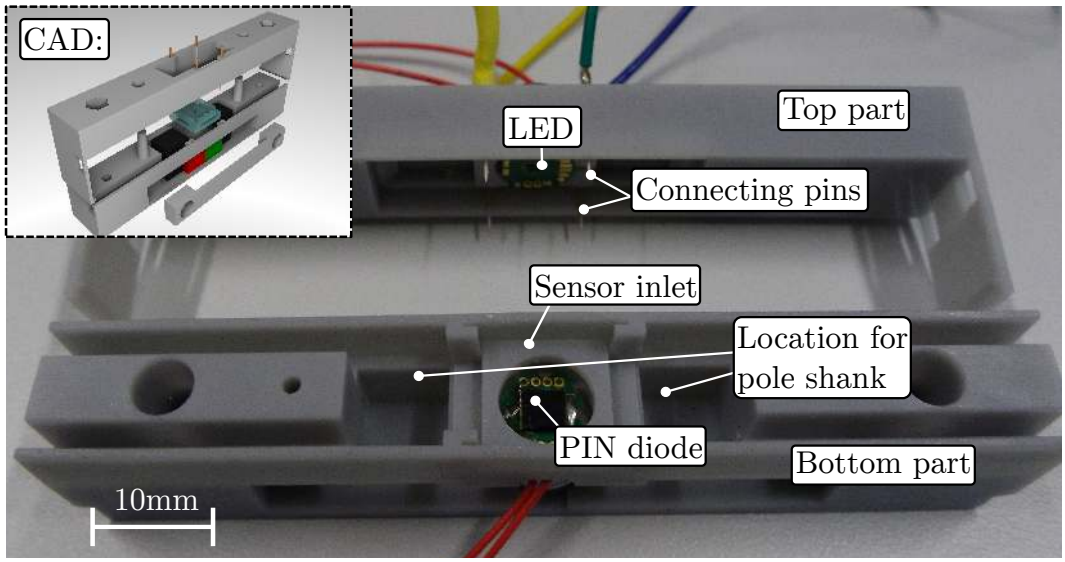

(b)

Figure 16: The measurement setup, including an oscilloscope, a excitation current source, power supply, the Lock-in amplifier for measuring the deflection equivalent output signal as well as the sensor's mounting device is depicted in (a). (b) shows the custom made mounting device disassembled.

4.4 Out-Of-Plane Magnetic Field Sensor

Two types of the proposed structures are depicted in Fig. 17. In addition to prototype oop_2 with 55-3D printed apertures, a prototype designed with 32-3D printed apertures with a particular size of 400×2000 µm was fabricated. Alternatively to the glass masks, flexible high resolution films (foils) with different gratings have been designed and ordered from 'micro lithography services' [41]. The advantage of these foils are low cost, fast manufacturing and no need for explicitly dicing. Further, the accessibility to create new glass masks with different aperture width is limited in the laboratories of ZISS[2], hence, high resolution films have been chosen.

Estimation of the Deflectable Structure's Mass
In order to estimate the structure's stiffness, both mass and the sensor's resonant frequency must be known. Unfortunately, no data about the density of the polymerised acrylic plastic is available from the manufacturer, but stated to be around $1200\,\mathrm{kg/m^3}$ in other references such as [42]. Hence, the structure's density is estimated by taking the volume from the CAD drawings and measuring the total mass of the whole device. Table 4 depicts results from different measurement approaches. The value of 158 mg is used to estimate the sensor's stiffness in subsection 4.4.2.

Method	m_{total} in g	ϱ_{calc} in $\mathrm{kg/m^3}$	m_{calc} in mg
Coarse scale	12	1183	153
Lab scale (1 sample)	0.34	1200	155
Lab scale (9 samples)	3.07	1220	158

Table 4: The coarse scale is a simple letter balance, with which the mass of different samples of polymerised acrylic plastic with known volume has been measured. The more precise measurement was conducted with a lab scale of type 'Sartorius'. For density estimation, the volume of the out-of-plane magnetic field sensor was extracted from the CAD drawings with an overall volume of $279.8\,10^{-9}\,\mathrm{m^3}$ and a deflectable part of $129.5\,10^{-9}\,\mathrm{m^3}$. The calculated densities agree very well with the stated density of $1200\,\mathrm{kg/m^3}$ for polymerised acrylic plastic.

4.4.1 Comsol Simulation

The natural frequency of interest in x-direction of prototype oop_1 and oop_2 was simulated using COMSOL Multiphysics. The shapes of the eigenmodes are depicted in Fig. 18. Acrylic plastic was selected from the Comsol built-in material library for the simulation, including material density of $1200\,\mathrm{kg/m^3}$ and a Young's modulus of 1420 MPa.

[2] Zentrum für Integrierte Sensorsysteme (Wiener Neustadt).

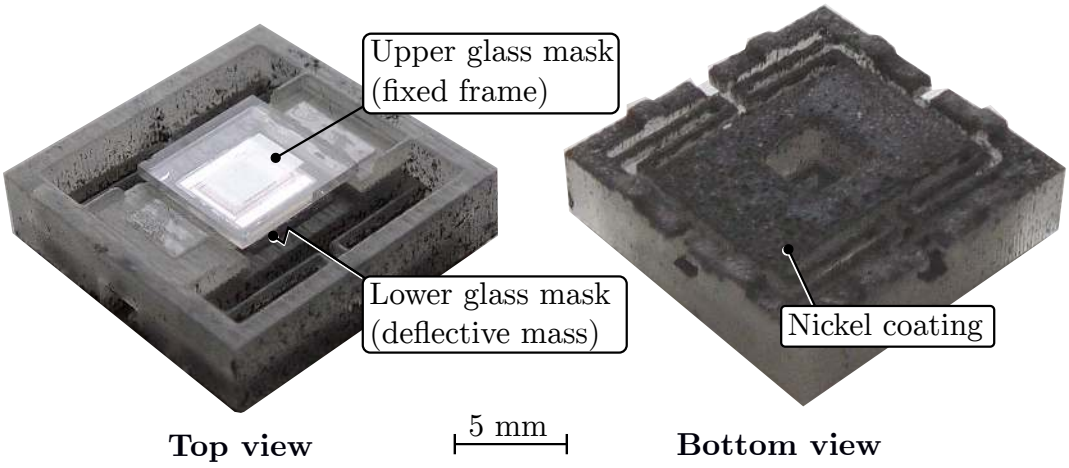

(a) Prototype 'oop_1'

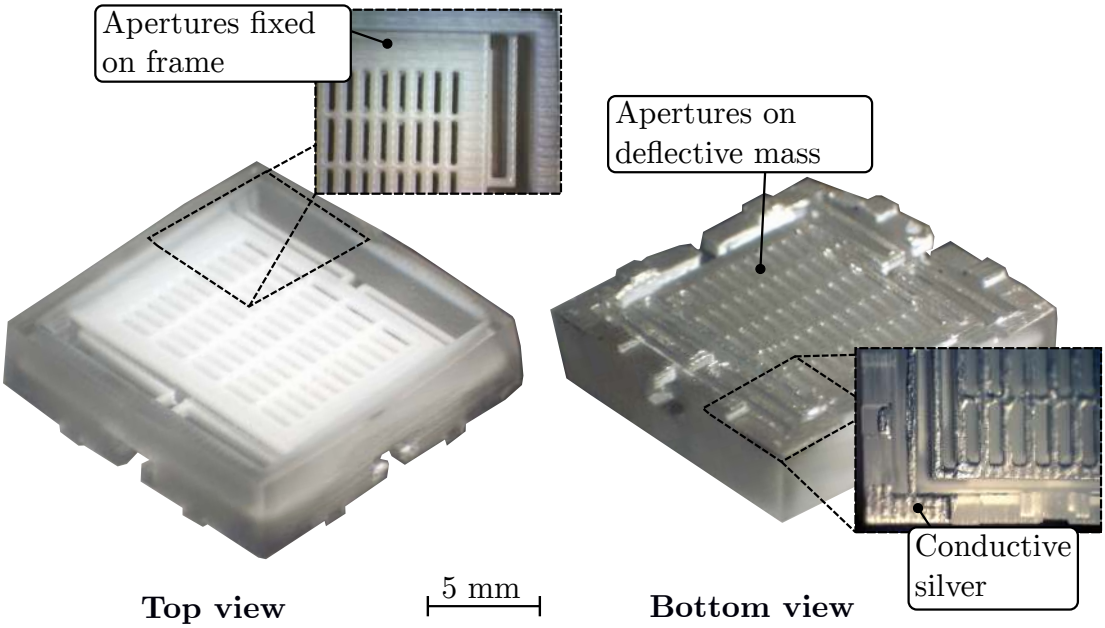

(b) Prototype 'oop_2'

Figure 17: 3D printed out-of-plane magnetic field sensor assembled with glass masks (a). Residues from the Nickel spray coating can be seen at the structure's side walls. These, however, do not compromise the functionality of the prototype. (b) model designed with 55-3D printed apertures with a particular size of 300×1700 µm and painted with conductive silver.

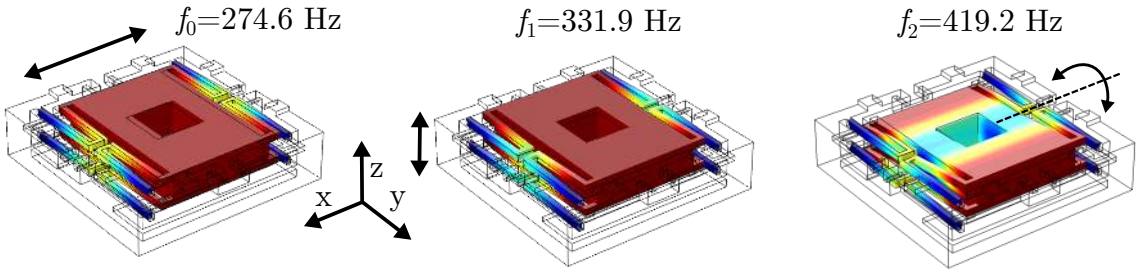

(a) Prototype oop_1

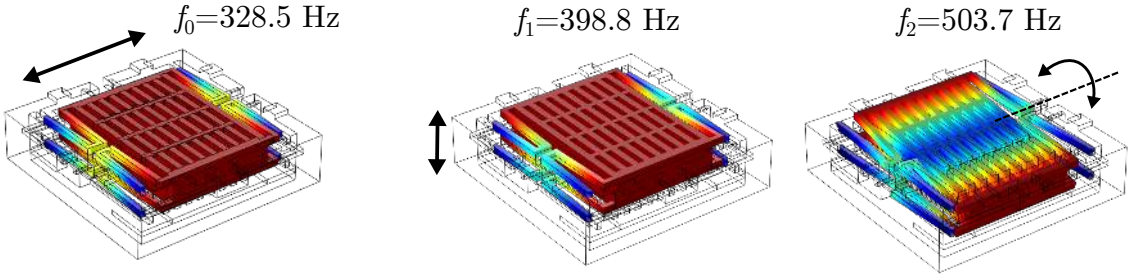

(b) Prototype oop_2

Figure 18: (a) FEM simulation results of the first three eigenmodes of prototype oop_1. The first eigenfrequency occurs as in-plane movement at 274.6 Hz, the second as out-of-plane movement at 331.9 Hz, the third as rotation at 419.2 Hz (from left to right). The simulation includes the mass of the bonded glass chip and the conductive coating. (b) Model oop_2 consists of 32-3D printed apertures with a size of 400 x 2000 µm. The mode of interest, i.e. the translation in x-direction occurs at 328.5 Hz, whereas the second and third mode occur at 398.8 Hz and 503.7 Hz, respectively.

4.4.2 Sensitivity Measurement

The sensitivity of the magnetometer is measured by applying different magnetic fields to demonstrate a linear behavior of the output signal. Therefore, the distribution of the magnetic flux density between neodymium disc magnets is characterised with a transversal Hall effect sensor (AS-NTM-2, 'Projekt Elektronik GmbH Berlin'). The sensor has a sensitive area of 0.12 mm^2 and measures the perpendicular component of the magnetic flux density, up to 2 T. The measurement setup is depictied in Fig 19.

Magnet-type	B in mT
S-12-01-N	24
S-12-02-N	51
S-12-03-N	73
S-12-05-N	119
S-12-06-N	150

Table 5: The table lists the different magnets and the associated averaged measured flux densities. A more detailed description of the magnets can be found in appendix A.

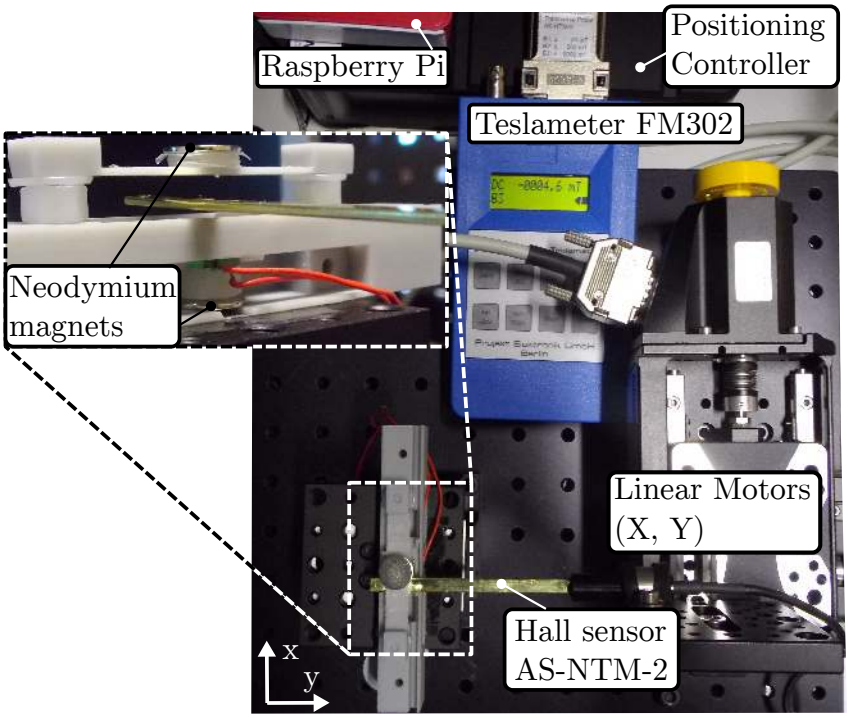

Figure 19: Measurement setup for automated magnetic field characterisation. A raspberry pi computer controls the Teslameter Hall sensor and 'Micos SMC Corvus ECO' positioning unit for the linear stages. The sensor element is located at the tip of the brass bar and adjusted to the height where the out-of-plane magnetic field sensor experience the field. The linear stages (PLS-85) have a resolution of 0.5 µm.

Figure 20 shows the partly opened mounting device with a sensor as well as the distribution of the magnetic flux density in and around the sensor. Even though the sensor's mass is fully coated with an electric conductor, it can be assumed that an applied current will take a path with the least resistance, hence the shortest path. This area is figuratively marked gray in Fig. 20b and highlights the zone in which the magnetometer experiences the Lorentz force. The magnetic flux density along the edges was averaged for five different magnets of different strenghts and summarised in Table 5.

Figure 21 depicts measurement results for an out-of-plane magnetic field sensor with 3D printed $400 \times 2000\,\mu m^2$ apertures (model 'ip_2'). Slight differences in the sensor's resonance frequency and, consequently, quality factor can be observed. Non-linearities and tensions introduced by the spring probe pins might be the causes of such frequency shifts. The quality factor was calculated from the parameters obtained by a fit to the transfer function, using the $-3\,dB$ *bandwidth method*.
Figure 22 depicts the structure's linear behaviour depending on the magnetic field strenght. The sensitivity is calculated from the measured data set in two different

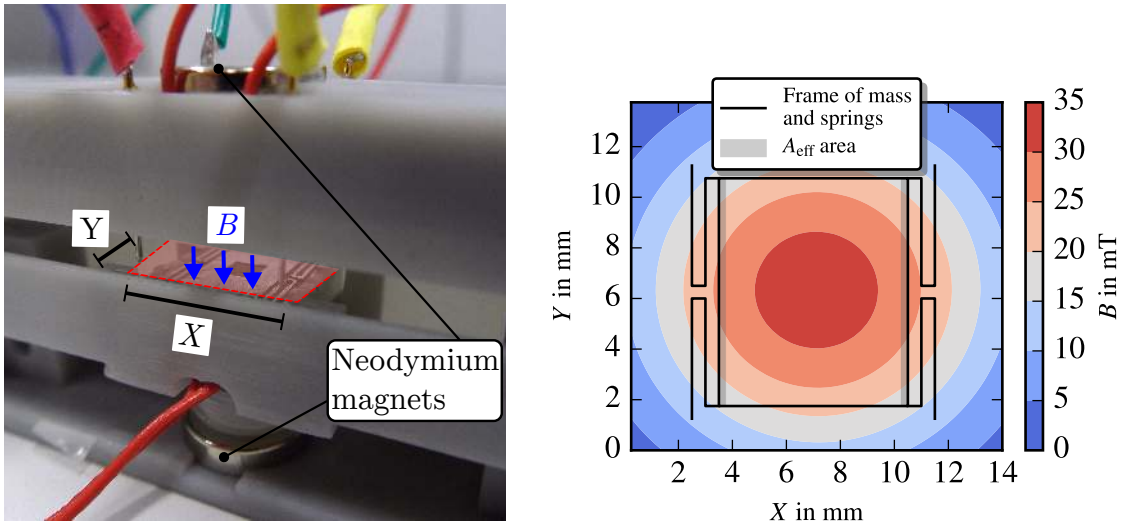

(a) (b)

Figure 20: (a) depicts a measurement setup of the out-of-plane magnetic field sensor inbetween two neodymimum disc magnets and partly opened top. The red area indicates the area of the measured magnetic field. (b) shows the distribution of the magnetic flux density, produced by neodymium disc magnets with 770 g strenght and characterised with Hall probe. A_{eff} highlights the magnetometer's effective 'sensing' area.

ways. The first approach considers the measured voltage at the structure's natural frequency, yielding a sensitivity of $S_{\text{f}_0} = 146.25\,\text{mV/T}$. The second approach yields a minimum sensitivity of $S_{\text{min}} = 6.83\,\text{mV/T}$, by extracting the output voltage at the low frequency range ($\omega \ll \omega_0$). Averaging the quality factor and multiplying it with S_{min} yields a sensitivity of $S = 176.92\,\text{mV/T}$. This solution differs from S_{f_0} due to possible non-lineartiy effects, multiplication with the averaged quality factor, the approach of fitted transfer functions, influence of noise and a chosen low frequency range which is too close to the sensor's resonant frequency ($\omega_{\text{min}}/\omega_0 = 0.42$).

The sensitivity depends on the position of which it is extracted from the transfer function. The sensitivity and the transfer functions of an ideal ideal driven damped harmonic oscillator are depicted in Fig. 23. In this analytical approach, a quality factor of 50 is assumed and a set of excitation forces is applied. As in the measurement, the minimum sensitivity S_{f_2} was extracted at the low frequency range, multiplied with Q, and compared with the sensitivity S_{f_0} at the oscillator's resonant frequency. It can be seen that the harmonized S_{f_2} fits exactly with S_{f_0} when it is determined in the low-frequency range. Sensitivities evaluated in the vicinity of ω_0 (e.g. S_{f_1} in Fig. 23) are affected by the resonant peak.

The credibility of S_{min} and S_{f_0} of the measurement is affirmed with a coefficient of determination R^2 of 98.2 % and 97.3 %, respectively. This reveals a high dependency

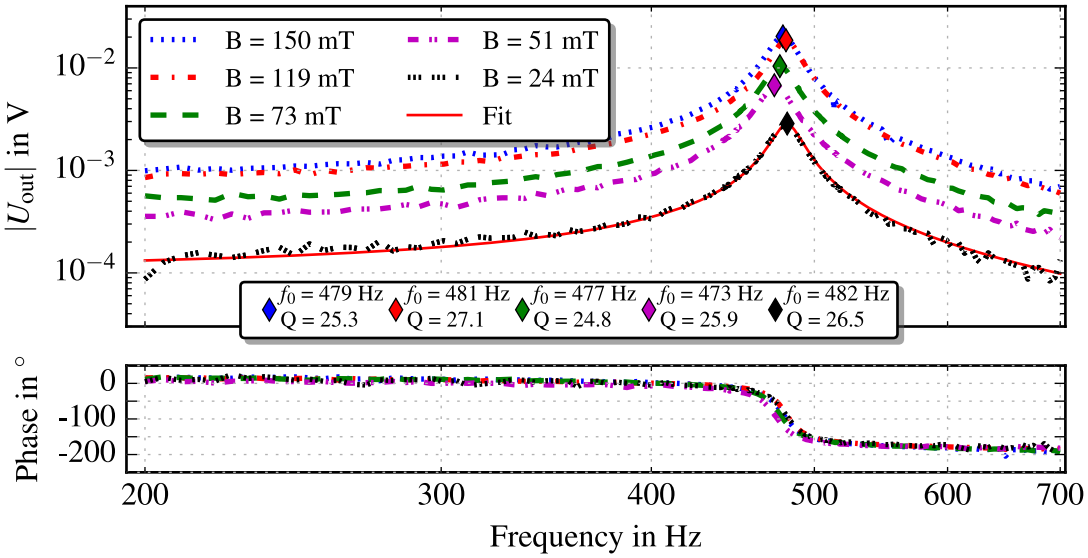

Figure 21: Measured transfer functions of an out-of-plane magnetic field sensor (model 'ip_2'). The applied excitation current was set to 20 mA (peak - peak) via a Keithley 6221 current source which correspondes to an RMS of 7.07 mA over a single spring. The different magnetic field strengths were provided by changing the magnets. All data have been fitted to extract the respective value of Q via the -3 dB *bandwidth method* and f_0, whereas only one fit curve is pictured for the sake of simplicity. The change of the magnetometer's natural frequency indicates non - linearities and tensions introduced by the spring probe pins.

between the change of an external magnetic field and the change of the sensor's output signal.
Furthermore, the magnetometer's stiffness is estimated to be $\bar{k} = 36\,\mathrm{N/m}$, by taking the calculated mass of 158 mg and the averaged natural frequency of which the data is depicted in Fig. 21.

Figure 22: Measured output voltage versus magnetic field to estimate the sensor's sensitivity. The data of $A_{\mathrm{f_0,\,fit}}$ and $A_{\mathrm{min,\,fit}}$ were extracted from the fitted transfer functions, whereas $A_{\mathrm{f_0,\,data}}$ and $A_{\mathrm{min,\,data}}$ are the measured values at the structure's resonance frequency and at 200 Hz, respectively. The data sets at 200 Hz have been harmonized, hence multiplied with Q_{avrg}, to allow comparison with the data at resonance.

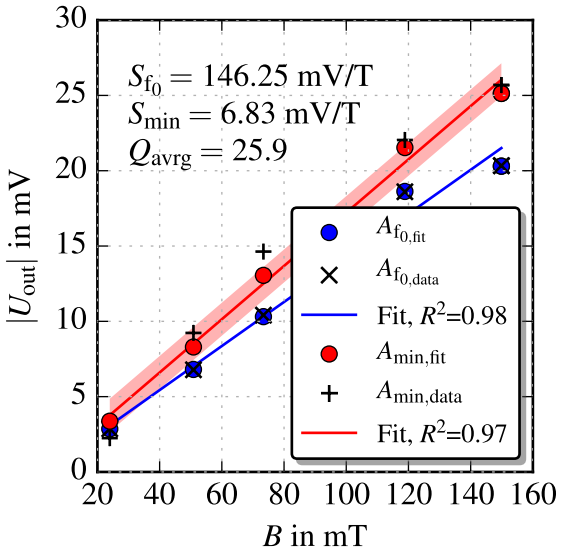

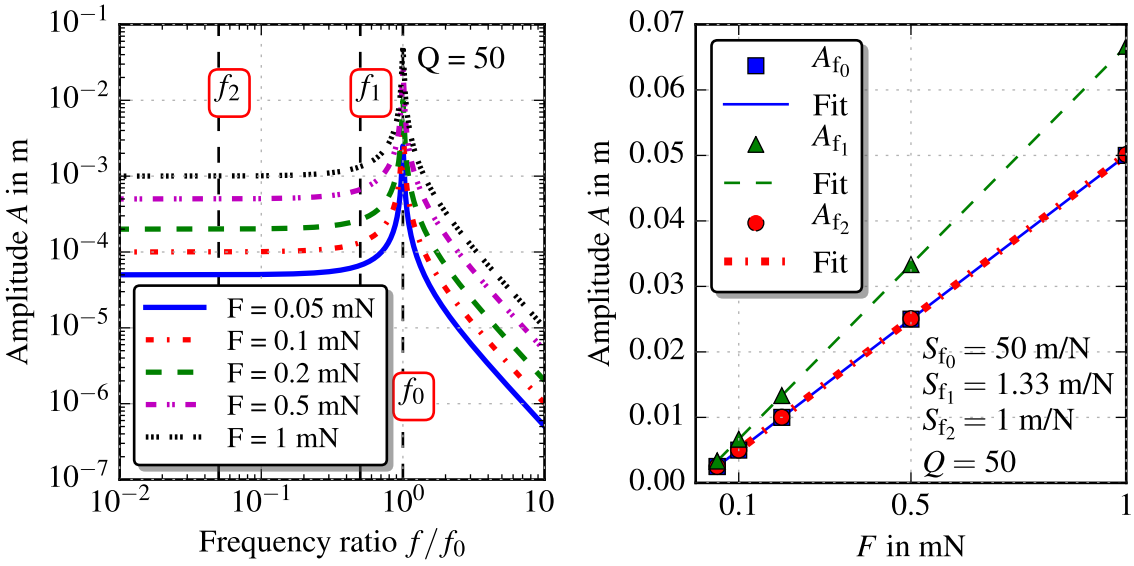

Figure 23: Transfer functions and sensitivity plots of a driven damped harmonic oscillator (analytical approach). The harmonised sensitivity $S_{\mathrm{f_2}}$ and $S_{\mathrm{f_0}}$ perfectly fits as depicted on the right, whereas the harmonised sensitivity $S_{\mathrm{f_3}}$ deviates due to the influence from the resonant peak.

4.4.3 Effect of Different Aperture Width

To overcome the phenomenom of light diffraction as discussed in Subsection 4.1.4, masks with large aperture width may be used. Different masks on prototype 'oop_1' are compared in Fig. 24, where a trend of increased output signal, i.e. sensitivity, for enlarged aperture width is observed. Although the same kind of structure has been used, the frequencies vary within 70 Hz, which indicates printing uncertainties and possibly wax residues contributing to some additional damping. This is affirmed by taking a closer look at the red dashed line corresponding to the 100 µm mask. There, the quality factor deviates 28 % from the averaged Q value. How wax residues affects the frequnecy and quality factor, can be found in more detail in Appendix B.

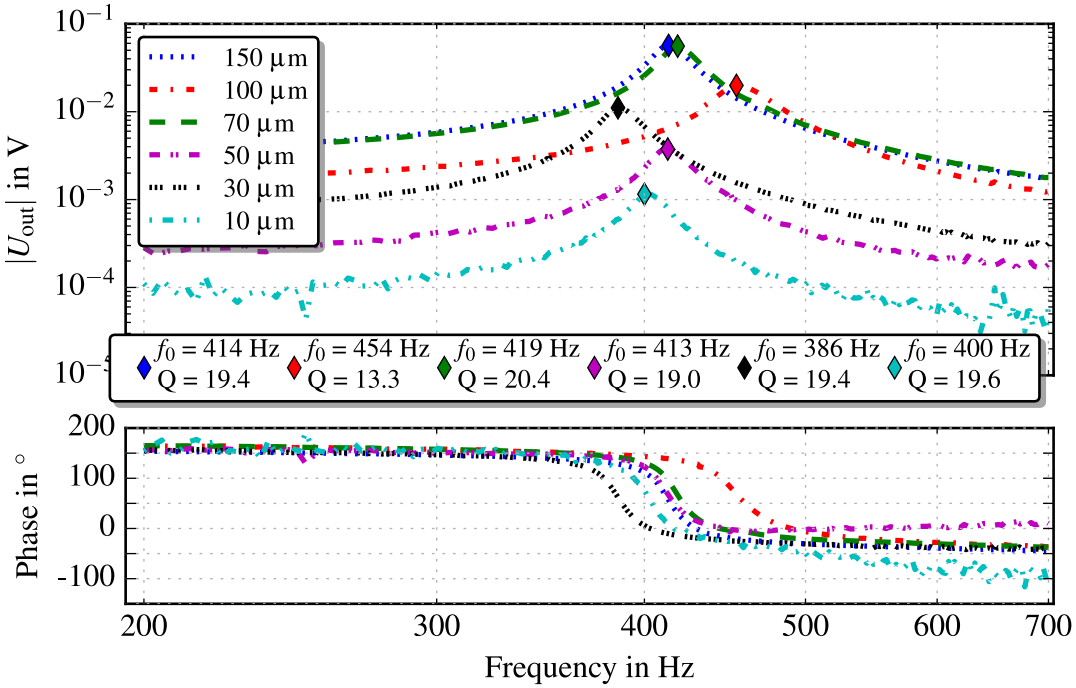

Figure 24: Comparison of prototype 'oop_1' with masks of different aperture width. The excitation current was set to 20 mA (peak - peak) and a magnetic field of 73 mT (magnet S-12-03-N) was applied. The second plot (model 'oop_1_100µm') clearly deviates from the other measurements.

4.4.4 Effect of Mask Alignment

Masks with different aperture width have been designed and manually glued onto the deflectable mass and fixed frame of prototype 'oop_1'. However, difficulties arise during the alignment process. Ideally, the apertures of the first mask are shifted by 50 % with respect to the other. This ensures that half of the light flux passes when the structure is idle.

Manual alignment affects the ouput signal as shown in Fig. 25 and Fig. 26. The plots in Fig. 25 depict always the same sample, by which the mask on the fixed frame was attached with adhesive tape to provide simple exchangeability. The same mask had been detached and subsequently reattached onto the frame to obtain varying adjustment. Two cases were considered in this context. In this case (case 1 in Fig. 25),

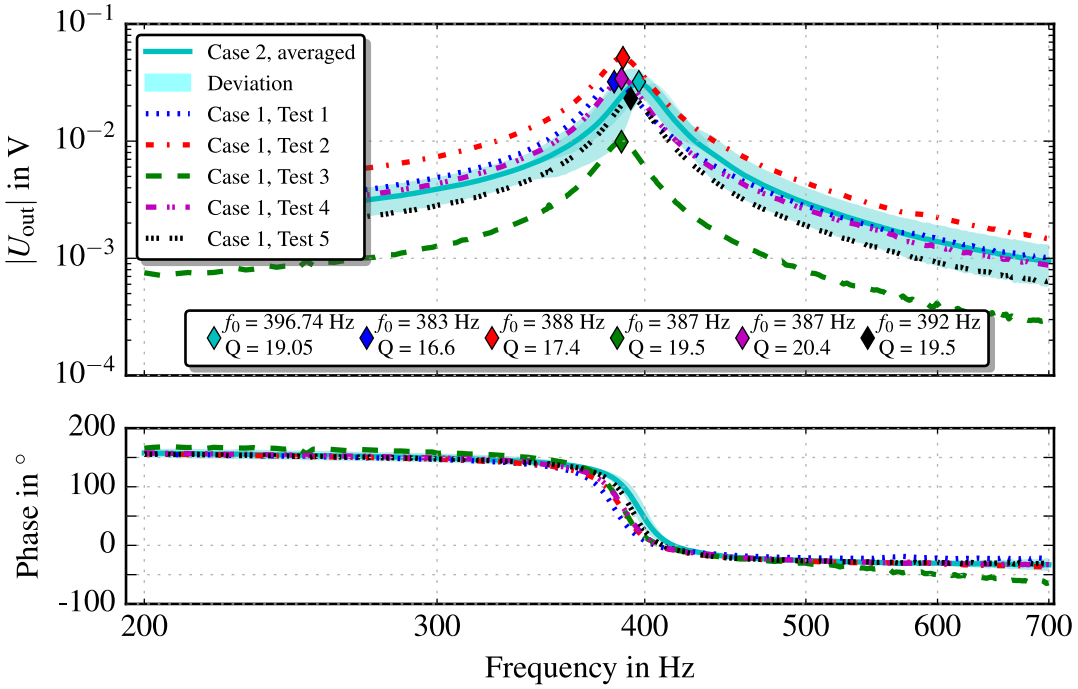

Figure 25: Measurement results for two different cases, using the same 3D printed structure of prototype 'oop_1' with attached foil mask of 70 µm slit width. The mask on the fixed frame in case 1 had been attached randomly, whereas in case 2, a more accurate mask alignment was aspired. The solid line denotes the averaged transfer function of five measurements. The associated deviation indicates an improvement of measurement results when the upper mask is more precisley aligned. The excitation current was set to 20 mA (peak - peak) and a magnetic field of 73 mT (magnet S-12-03-N) was applied.

the mask was attached randomly and rotational misalignement was accepted. The second case focused on more accurate alignment, where rotational misalignement was prohibited and an almost identical mask offset was aspired. In this way, occuring interference patterns from those two masks had been observed and the top mask adjusted until these interference vanished. This approach led to high repeatability of the output signal compared to the random alignment of the first case.
Additionally, five samples of model 'oop_1' have been, rather randomly, attached with the same mask type. The results are depicted in Fig. 26, showing different frequencies and output signals. As discussed in Subsection 4.4.3, this might be the effect of 3D printing uncertainties and possible wax residues.

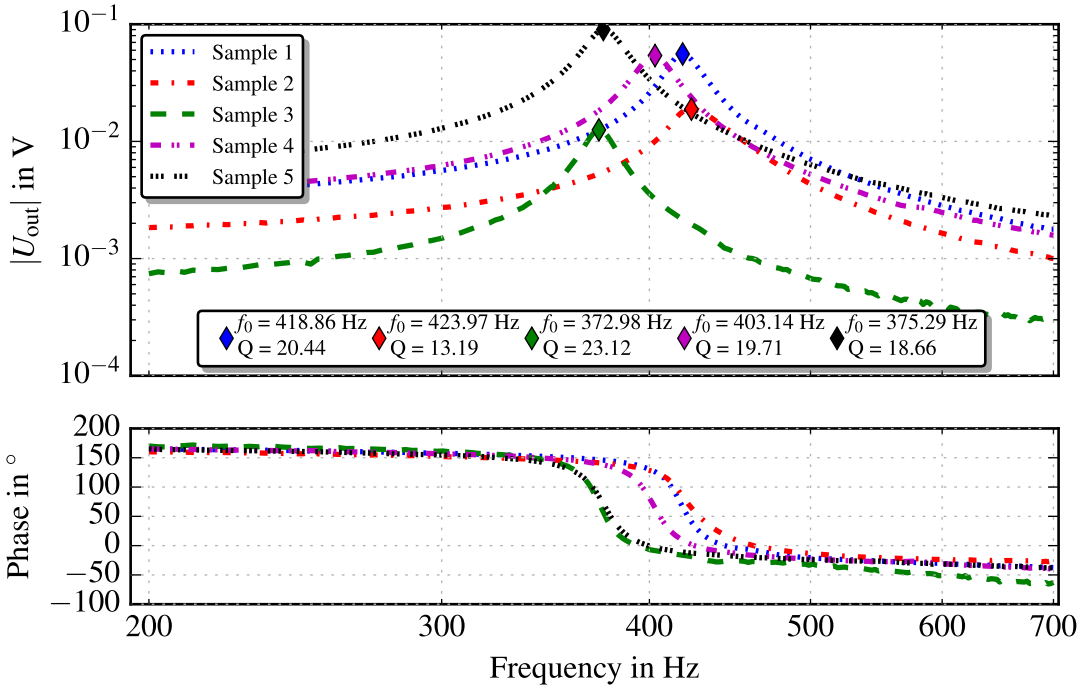

Figure 26: Five samples of prototype 'oop_1', attached with foil masks of 70 µm slit width, are compared, yielding different frequencies and output signals. The measurement settings were the same as for Fig. 25.

4.4.5 Temperature Dependence

Polymers are strongly temperature-sensitive which challenges the design of reliable 3D printed MEMS. Temperature affects rearrangement processes of molecules in polymer materials, e.g. an increase of the temperature accelerates relaxation processes and also induces a change of the structure's dimensions due to thermal expansion of the material. Thus, the Young's modulus is expected to decrease yielding a shift of the resonant frequency [43]. Furthermore, the coefficient of thermal expansion also depends on the temperature dramatically. Some values of the coefficient of thermal expansion α_{th} are listed in Table 6[3].

Material	α_{th} **(linear) in** $10^{-6}/$**°C around 20°C**
Silicon	2.6
Copper	16.7
Polymers	50-200

Table 6: Comparison of the coefficient of thermal expansion for three materials, valid for a temperature around 20 °C.

Figure 27 depicts a measurement setup for temperature characterisation of the out-of-plane magnetic field sensor in a climatic test chamber. The measurement was conducted at a temperature range of 5-50 °C, resulting in a frequency shift due to softening of the polymer and thermal expansion of the material (Fig. 28). The relative change of the resonant frequency is fitted with linear functions and could be heuristically partitioned in a range $T \leqq 25$ °C and $T > 25$ °C. However, in this thesis the emphasis was laid on a rapid prototyping approach to explore proofs of concept for new sensor designs, thus deeper investigations must be conducted to yield a more credible result about the sensor's temperature dependnce.

[3] values obtained from http://cleanroom.byu.edu/CTE_materials

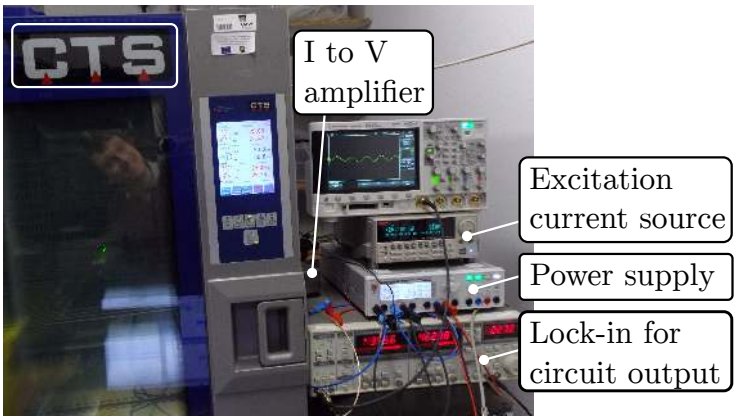

Figure 27: Measurement setup consisting of the clima temperature system (CTS) which enables temperature and humidity characterisation from −20 °C to +180 °C and 10 − 98 % relative humidity.

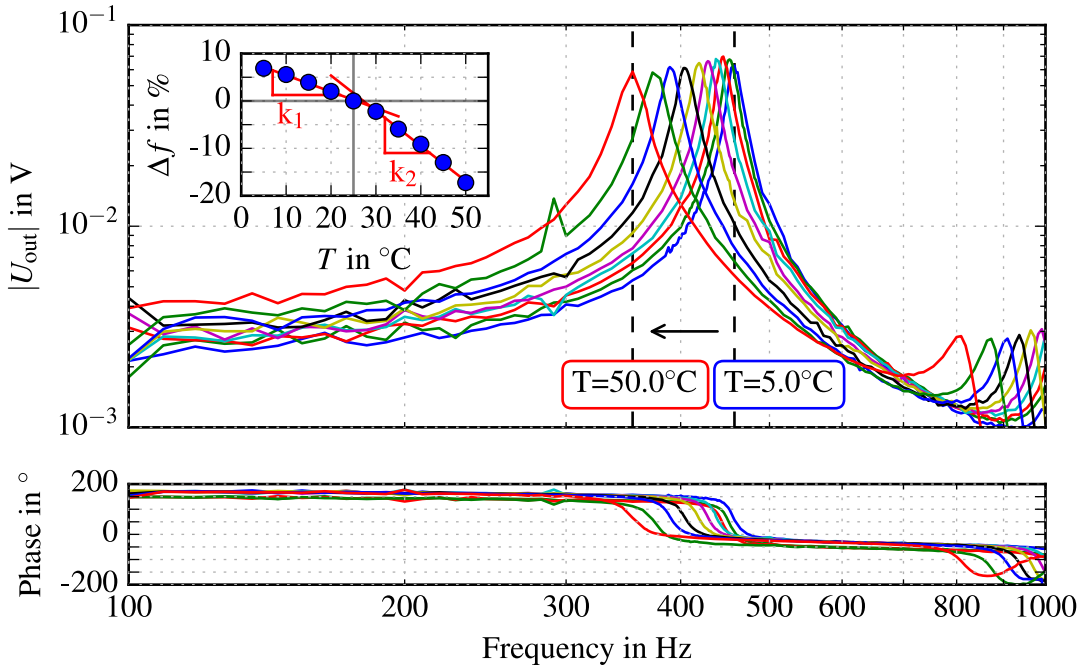

Figure 28: Measurement results of the temperature dependence of prototype 'oop_1' attached with a foil mask of 70 µm slit width. Starting from 5 °C the temperature was increased in steps of 5 °C up to 50 °C at a set relative humidity of 50 %. A frequency shift from 458 Hz to 355 Hz corresponding to a Q shift of 27 to 17, respectively, was measured. The frequency range at this measurement has been extended yielding an additional resonant peak around 900 Hz corresponding to the structure's higher eigenmode. The inset shows the relative change of the resonant frequency calculated for a reference temperature $T_0 = 25\,°C$. The frequency shift can be approximated with a linear fit between 5-25 °C and 30-50 °C corresponding to a measured frequency shift of $k_1 = -0.35\,\%/°C$ and $k_2 = -0.74\,\%/°C$, respectively.

4.5 In-Plane Magnetic Field Sensor

Two types of proposed structures are depicted in Fig. 29.

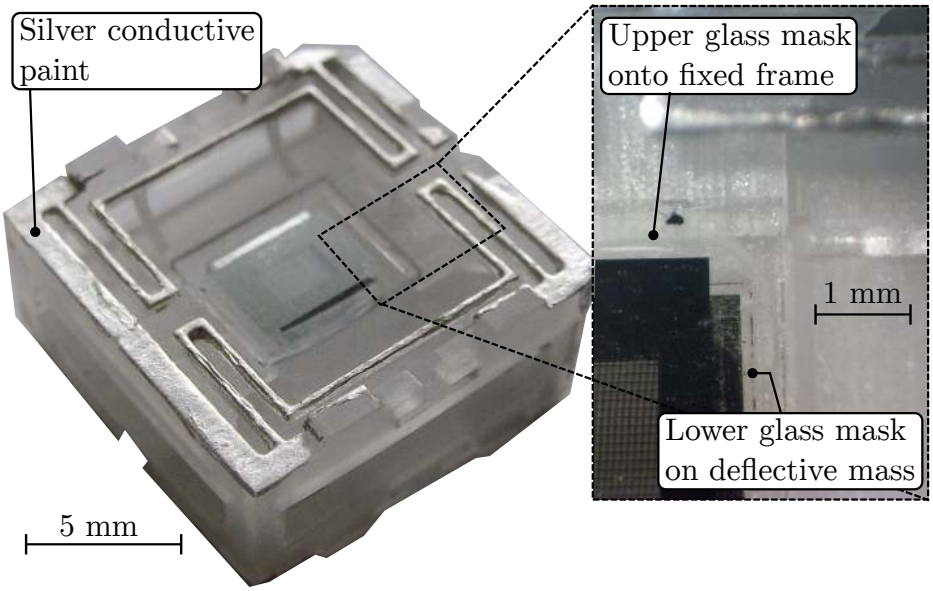

(a) Prototype 'ip_1'

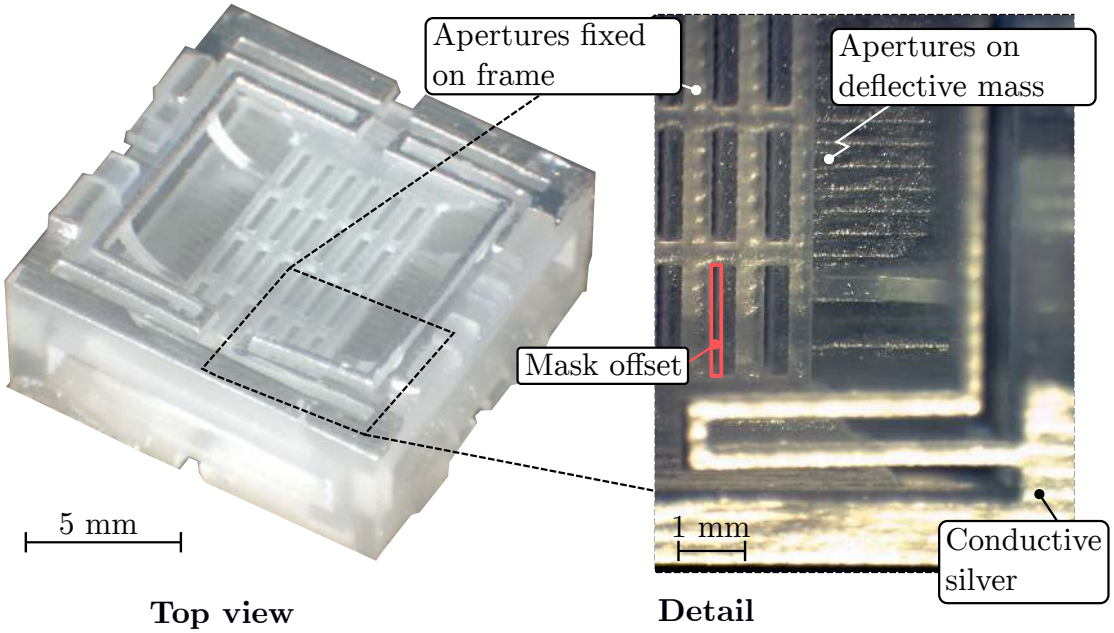

(b) Prototype 'ip_2'

Figure 29: (a) 3D printed in-plane magnetic field sensor assembled with glass masks and coated with silver conducting paint. (b) model designed with 24 apertures with a size of $400 \times 1700\,\mu m^2$ and partly coated with conductive silver. The red frame marks the mask offset, through which the light flux passes.

4.5.1 Measurement Results - Sensitivity

A magnetic field is established between two pole shanks which are connected via neodymium magnets. This provides easy access for changing the magnets. The distribution of the magnetic flux density between the pole shanks is measured with a Hall sensor, in a similar way as mentioned in Subsection 4.4.2. A more detailed description about the measurement setup can be found in Appendix C. Figure 30a depicts the assembled setup for characterising a resonator featuring the subjacent magnets and pole shanks, whereas Fig. 30b highlights the 'pseudo'-horizontal magnetic field distribution between the poles.

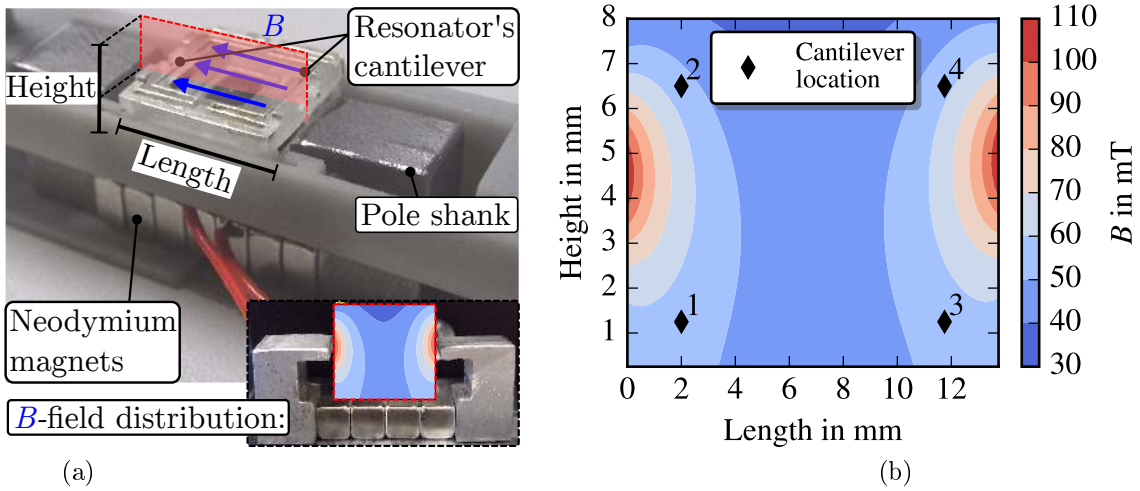

(a) (b)

Figure 30: (a) depicts a measurement setup of the in-plane magnetic field sensor among two pole shanks, where the top part with the connecting pins is not shown. The red area indicates the upper part of the measured magnetic field. (b) shows the distribution of the magnetic flux density between two pole shanks, produced by neodymium block magnets with a strength of 1500g . The characterisation of the B-field has been carried out with a transversal Hall probe (Teslameter FM 302), which measures the perpendicular component of the magnetic flux density. The cantilevers of the 3D printed resonator experience the field at certain locations, which are marked with diamonds 1-4.

The magnetic flux density experianced by the indivdual cantilevers was extracted from the contour plots and summarised for a set of magnets in Table 7.
Figure 31 depicts the measured transfer functions and a fit of one of the curves. The field distribution between the pole shanks indicates an inhomogeneous magnetic field. This is due to the geometry of the setup and affects the measurement in a way that two peaks have been observed. In an idealised environment, assuming that the applied magnetic field is horizontally aligned to the cantilevers, only one distinct resonant peak might be measured corresponding to one distinct mode. A second peak might occur in the presence of a heterogeneous or rotated magnetic

	Cantilever				
Magnet type	♦1	♦2	♦3	♦4	
W-05-N	25.0	25.9	24.5	26.2	
S-06-01-N	37.2	37.5	38.7	38.0	
Q-10-05-03-N	54.1	55.2	57.0	55.7	
Q-10-05-1.5-G	60.0	62.8	62.8	61.5	
Q-19-13-06-LN	90.4	89.5	87.0	91.1	

B in mT

Table 7: Different magnet types and their corresponding measured magnetic field strength, extracted at the structure's cantilever locations.

field. This is discussed in more detail in Subsection 4.5.2. The observed frequency shifts may arise from assembling and disassembling the mounting device, which is necessary to exchange the magnets and, hence, introduces tension from the clamping mechanism. Furthermore, the reproducibility of placing the pole shanks at the same location is limited due to the different sizes of the magnets and their geometry. Hence, improving the measurement setup is expected to yield better results.

A similar approach as in Subsection 4.4.2 has been conducted to approximate the sensor's sensitivity (Fig. 32). The fitted data strongly correlates with the measured one at resonance, whereas the data at the low-frequency domain significantly deviates from the fit and also does not linearly depend on a changing magnetic field. The behaviour at the low-frequency domain is not fully understood and is still under investigation. Hence, the minimum sensitivity S_{min} cannot be estimated at the moment.

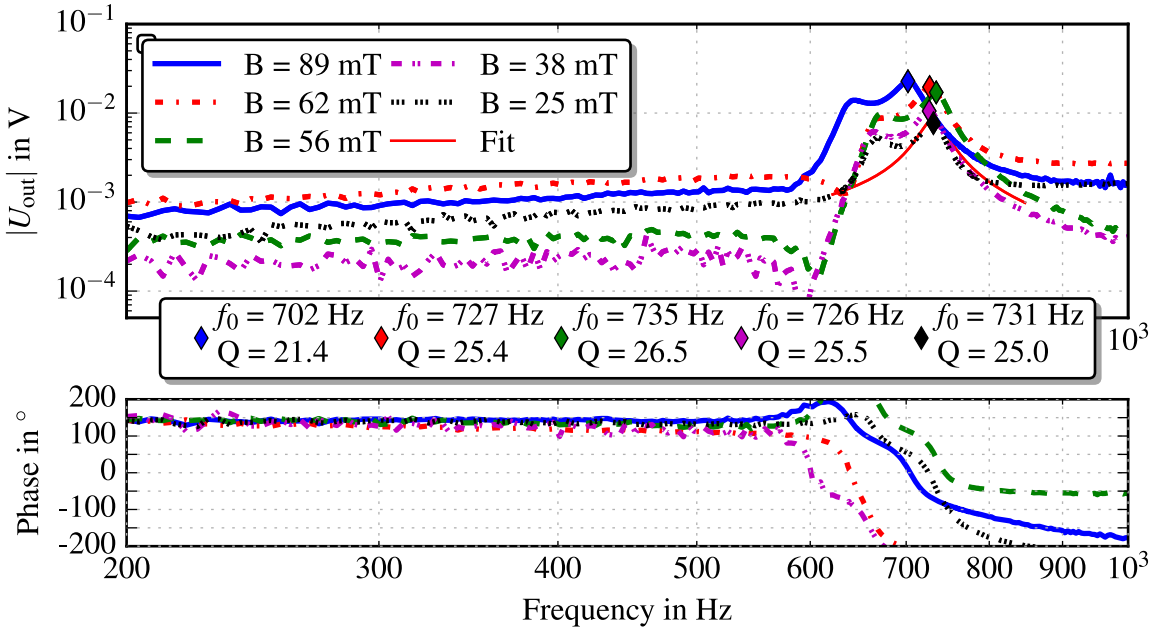

Figure 31: Measured transfer functions of an in-plane magnetic field sensor (model 'ip_2'). The applied excitation current was set to 20 mA (peak-peak) and a set of magnetic field strengths was applied. The diamonds indicate the structure's natural frequency. Comparing the measured deflection-equivalent output signal with COMSOL simulation results from Fig. 35, clearly illustrates the effect of an inhomogeneous magnetic field, defined by two distinct resonant peaks. The simulation significantly differs from the measurement due to material uncertainties and non-linearities. The resonant peaks of interest have been fitted to approximate the Q value via the -3 dB *bandwidth method*.

Figure 32: The figure on the right depicts the measured output versus magnetic field and linear fit at the structure's resonant frequency.

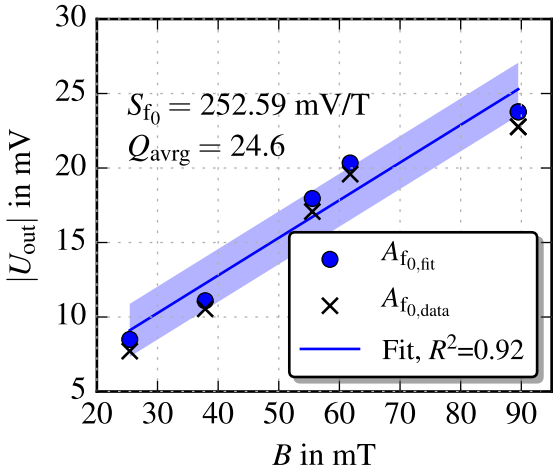

4.5.2 Comsol Simulation

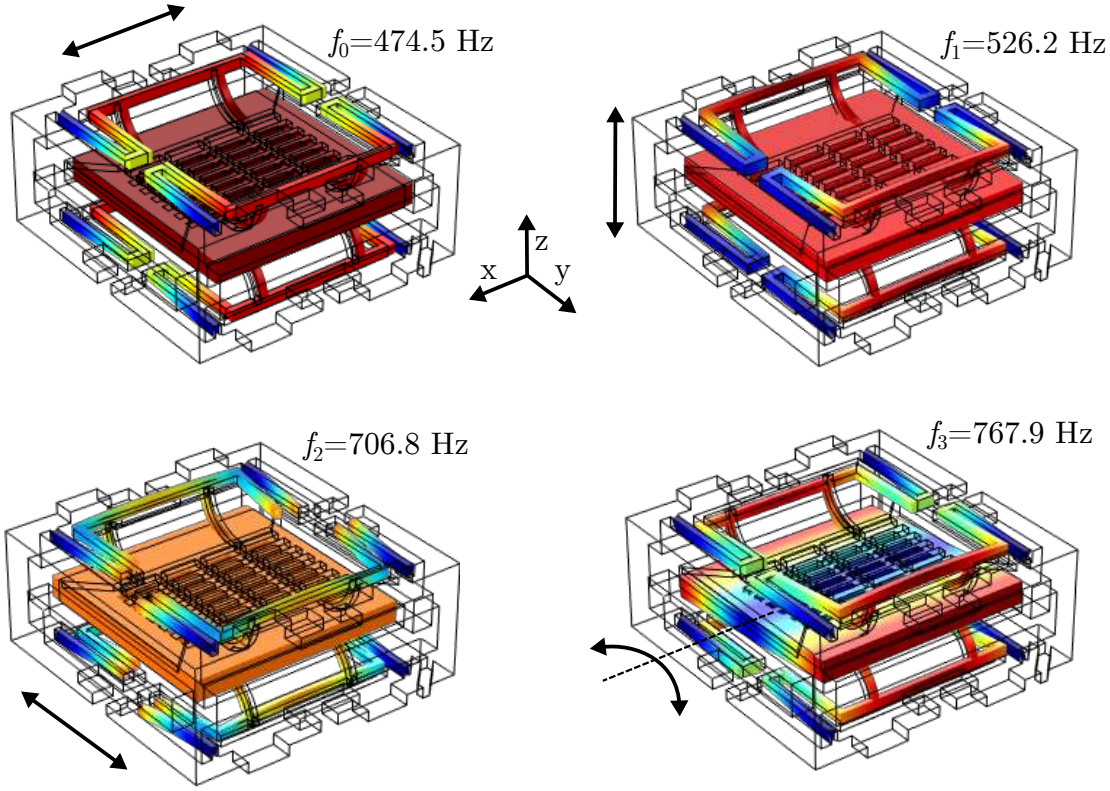

Figure 33: FEM Simulation results of the first four eigenmodes of model prototype 'ip_2'. The first eigenfrequency occurs as in-plane movement in x-direction at 474.5 Hz, the second as out-of-plane movement at 526.2 Hz, the third as (the desired) in-plane movement in y-direction at 706.8 Hz, the fourth as rotational mode at 767.9 Hz.

The in-plane magnetic field sensor exhibits two distinctive eigenmodes both of which result in an in-plane movement of the mass (Fig. 33), where the desired frequency for the movement in y-direction was simulated to be 706.8 Hz. As in Subsection 4.4, the additional mass of the silver conductive lead was considered during simulation.

Due to the structure's complex design and specific method of excitation, additional simulations were conducted to explain the phenomenon of the two occurring resonant peaks observed during the measurements. Hence, the model's behaviour has been simulated in two ways. First, in an idealised environment with a perfectly horizontally applied homogeneous magnetic field and, second, for a tilted magnetic field. The results for modly applied el 'ip_2' is depicted in Fig. 34, where an additional resonant mode appears in the presence of a tilted magnetic field.
These results do not completely agree with the measurement results from Subsec-

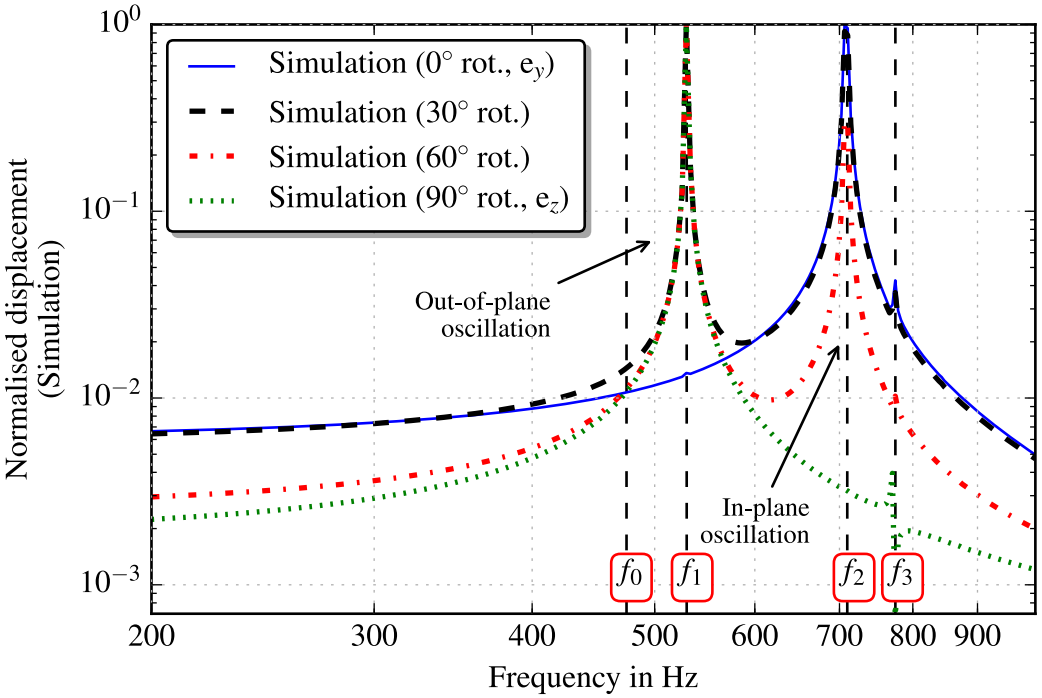

Figure 34: Simulation results of the structure's displacement for different external magnetic fields rotated in the yz-plane. When the magnetic field is horizontal (0 °), a distinct resonant peak at the frequency of interest (mode f_2) occurs. Another distinct peak appears at 526.2 Hz (f_1) when the field is 90 ° rotated corresponding to the out-of-plane oscillation. A fluent transition between those peaks is observed for intermediate field angles.

tion 4.5.1. Thus, the simulation was improved by simulating an external inhomogeneous magnetic field, approximately with the same field distribution as measured between the pole shanks (see Fig. 30b). Figure 35 depicts the simulation results of the magnetic flux density. This field distribution is used to simulate the deflection of the structure's mass, which is depicted in Fig. 37. The simulation differs from the previous one in a way, that the peak of the out-of-plane oscillation (f_1) almost vanishes. Instead, a new distinct peak occurs which corresponds to the rotational mode at f_3. Hence, the shape of the simulated transfer function corresponds very well with the measurement results from Fig. 31.

Figure 37 depicts a comparison of the sensor's transfer function between simulation, measurement of the modulated light flux and displacement measurement with a digital holographic microscope (DHM). Unfortunately, the sensor characterised in the former Subsection 4.5.1 had been damaged, therefore the prototype 'ip_1' attached with foil masks of 70 µm gratings was measured. Magnets of type 'Q-10-05-1.5-

G', yielding a magnetic field of 60 mT at the sensor's cantilevers were used and an excitation current of 20 mA (peak-peak) was applied. The setup for the displacement measurement is depicted in Fig. 36. All three transfer functions exhibit a similar shape, but differ in frequency of the observed modes. Tension introduced by the spring probe pins of the clamping mechanism might cause these frequency differences. The maximum in-plane and out-of-plane displacement of the sensor's mass was measured to be 148 nm at 693 Hz and 29 nm at 825 Hz, respectively. This corresponds very well with the simulation result which indicates an in-plane oscillation at the higher peak (f_2) and a mix of in-plane and out-of-plane oscillation, i.e. rotational mode at the lower peak (f_3).

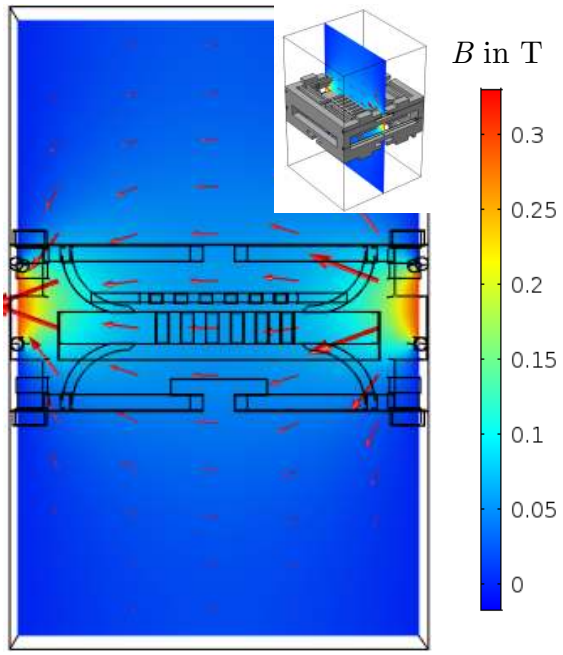

Figure 35: Simulation results of the heterogenous magnetic field corresponding to the measurement setup. Depicted is a single plane of the field distribution extracted at the structure's center. The red arrows are proportional in size of the magnetic field strenght and point in the direction of the magnetic field lines.

Figure 36: Measurement setup to quantify the deflection of the transducer's mass. The digital holographic microscope DHM®-R2100 (Lyncée Tec) is capable of optically measuring both in-plane deflection with pattern tracking and out-of-plane oscillation from phase images which reveal directly the surface topography with a sub-nanometre vertical resolution.

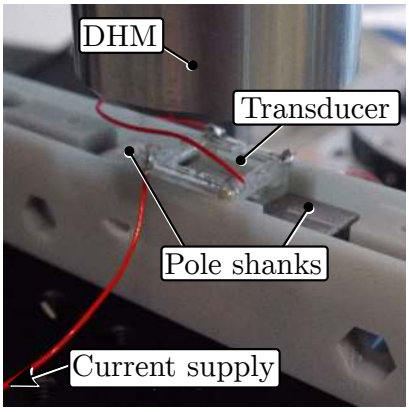

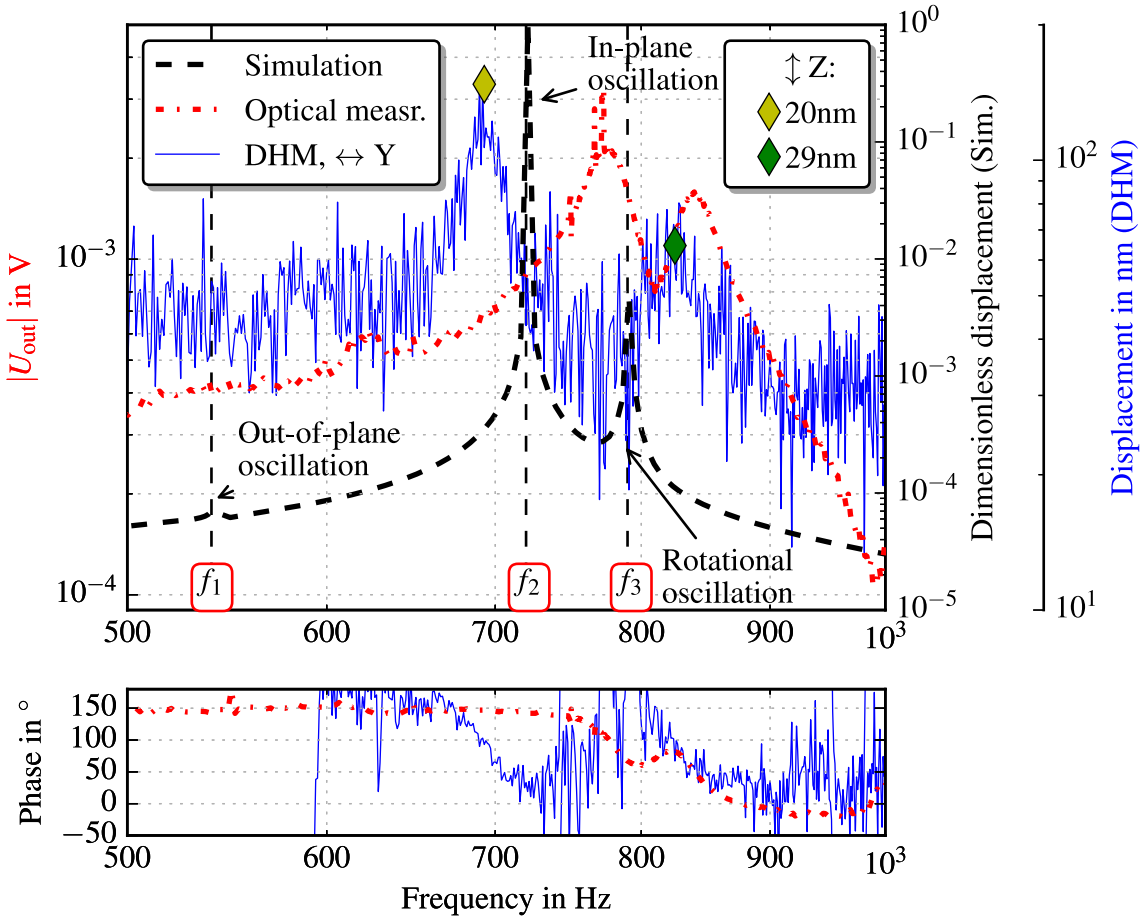

Figure 37: Comparison between simulation results (black dashed line), measurement with optoelectronics (red dashed-dotted line) and direct measurement results of the deflection of the transducer's mass (blue line). The blue line depicts results from pure in-plane deflection, whereas the diamonds mark the out-of-plane deflection at specific frequencies, both measured via the DHM. Nevertheless, the measurement of the out-of-plane deflections agree with the simulation and the green diamond indicates the largest oscillation where the structure exhibits tilting. Furthermore, the red dotted line differs from the blue one due to possible tension from the clamping mechanism.

5 Conclusion

The thesis highlights advantages of 3D print technologies in terms of fast design, accelerated testing phases and the possibility of creating complex geometries in contrast to costly re-design and fabrication cycles in traditional MEMS fabrication. In addition, rapid prototyping is useful as effective assessment tool to demonstrate working principles for designs before initiating costly MEMS technology. In this prospect, two unique designs for Lorentz force based magnetometers have been 3D printed with state-of-the-art Multijet Modelling (MJM) technology and characterised. The designs have been sequentially improved to reduce the amount of wax residues from the printing process. Additionally, different surface coatings have been tested to achieve the best possible surface conductivity.
The structure's sensing principle is based on light flux modulation from two stencil masks by relative in-plane movement which is detected by a photodiode. The mass's deflection is induced by Lorentz forces created at current carrying cantilevers in presence of a magnetic field. A custom made mounting device has been designed, providing access to and fast interchangeability of the magnets to characterise the structure's behaviour in a static magnetic field. The sensitivity of the in-plane and out-of-plane magnetic field sensor have been determined and summarised in Table 8.

	Magnetometer type	
Parameters	**out-of-plane**	**in-plane**
Sensitivity S_{f_0}	146.3 mV/T	252.6 mV/T
Sensitivity S_{min}	6.83 mV/T	-
excitation current	20 mA	20 mA
R^2 at f_0	0.982	0.917

Table 8: Parameter comparison of the in-plane and out-of-plane magnetic field sensors.

Furthermore, the effect of mask alignment and wax residues have been investigated. A good reproducibility of the output signal can be achieved, if rotational misalignment is prohibited and if the samples are sufficiently cleansed which increases the quality factor.

However, a major disadvantage of 3D printed MEMS resonators are the limitations due to currently achievable printing resolutions and the mechanical properties of polymer materials. Nevertheless, 3D printing technology has been proven to be sufficient for rapid prototyping and exploring proofs of concept for new sensor designs. Potential for further enhancement is given considering the ongoing development on the 3D printing market achieving even better resolution and higher printing accuracy, as well as developing new printable composite materials.
For future investigation, the mounting device is intended to be improved in order to

achieve a truly homogeneous B-field, which should verify the simulation results from Subsection 4.5.2. Finally, further experiments have to be conducted with both of the proposed designs assembled together with the necessary optoelectronic components. This way, in- and out-of-plane components of the magnetic field strength can be measured at the same time using a single LED and a large quadrant photodiode.
Future application of polymer materials in MEMS with 3D printing technology requires profound understanding of the polymer's properties. Investigation of the material's performance at low pressures shall be conducted to proof if the polymer structures outgas. This may stiffen the material, yielding a shift of the structures natural frequency. Exploring temperature dependency of 3D printed MEMS is necessary to understand the system's stability (thin current carrying cantilevers may strongly deform at high excitation currents). Furthermore, measurements identifying the effect of clamping loss, TED and material damping may contribute to a profound understanding about intrinsic limits of polymer MEMS.

Appendix A Neodymium Magnets

The neodymium magnets used for the characterisation of the magnetometers within this thesis are purchased from www.supermagnete.de and are summarised in more detail in Table 9. The entries in the column 'Note' comprises the aditional information: The letter 'N' indicates the maximum working temperature, which is at 80 °C, whereas the following number informs about the maximum energy product of the magnet. The energy product $E_{\max} = B \cdot H$ specifies the amount of magnetic energy stored in a magnet in units of $\mathrm{kJ/m^3}$. The numbers 42, 45 and 50 state an energy product of 318-334, 342-358 and 374-406 $\mathrm{kJ/m^3}$, respectively.
The hindmost number in the column 'Note' is the approximated adhesive force in unit gram, which was obtained under ideal test conditions and strongly depends on the magnet's geometry. The measurement procedure is conducted as follows: One pole of the magnet is glued onto a non-magnetic material with hook, whereas the other pole is attached onto a fixed steel plate. A pulling force is applied until the magnet separates from the plate, thus yielding the maximum adhesive force. For more information visit the vendors homepage www.supermagnete.de.

Out-of-plane magnetometer		**In-plane magnetometer**	
Magnet-type	**Note**	**Magnet-type**	**Note**
S-06-01-N	N45, 350 g	S-12-01-N	N42, 770 g
Q-10-05-1.5-G	N50, 980 g	S-12-02-N	N45, 1600 g
W-05-N	N42, 1100 g	S-12-03-N	N45, 2500 g
Q-10-05-03-N	N45, 1500 g	S-12-05-N	N45, 3300 g
Q-19-13-06-LN	N42, 4100 g	S-12-06-N	N45, 3900 g

Table 9: Summary of the set of neodymium magnets, used within this thesis.

Appendix B Wax Residues

A drawback of the 3D printing technique based on liquid resin is the necessity for supporting wax which may remain in poorly designed cavities. Those waxy residues affect the moveable mass in terms of frequency shift and lower Q value due to increased friction. Figure 38 depicts measurement results of prototype 'oop_1_20µm_foil' and 'oop_1_30µm_foil' with wax residues and after cleaning the gap between frame and moveable mass with a tweezer. The wax residues contribute not only to additional damping, but also introduce tension, which may be the effect of the wax's high viscosity.

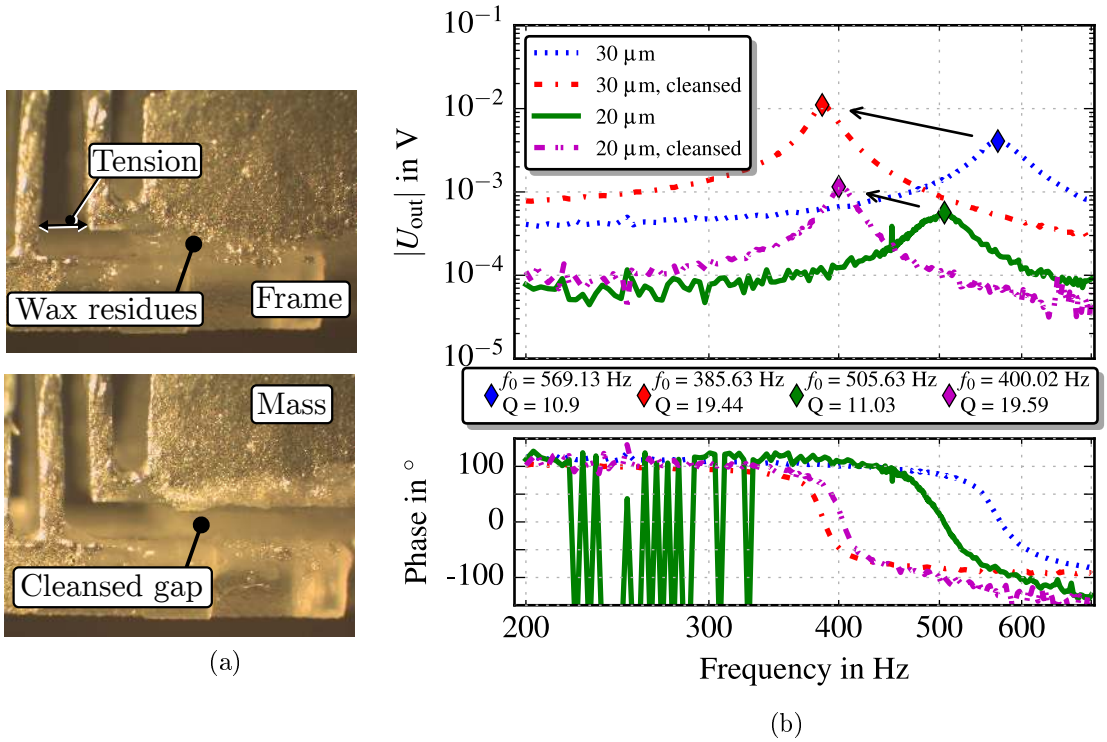

(a) (b)

Figure 38: (a) Micrograph of the out-of-plane magnetic field sensor with wax residues which introduce tension and a relaxed mass after cleaning. (b) The corresponding measurement results for samples with attached foil masks of 20 µm and 30 µm are depicted. The excitation current was set to 20 mA (peak - peak) and a magnetic field of 73 mT (magnet S-12-03-N) was applied. An increased quality factor and frequency shift to the left is observed which is marked with an arrow.

Appendix C Measurement Setup - Field Distribution between Pole Shanks

Figure 39 depicts the measurement setup for automated magnetic field characterisation between two poles. A Hall probe is fixed to linear stages with two degrees of freedom to characterise the magnetic field in the yz-plane. The linear stages (PLS-85) are capable to travel in 0.5 µm steps.

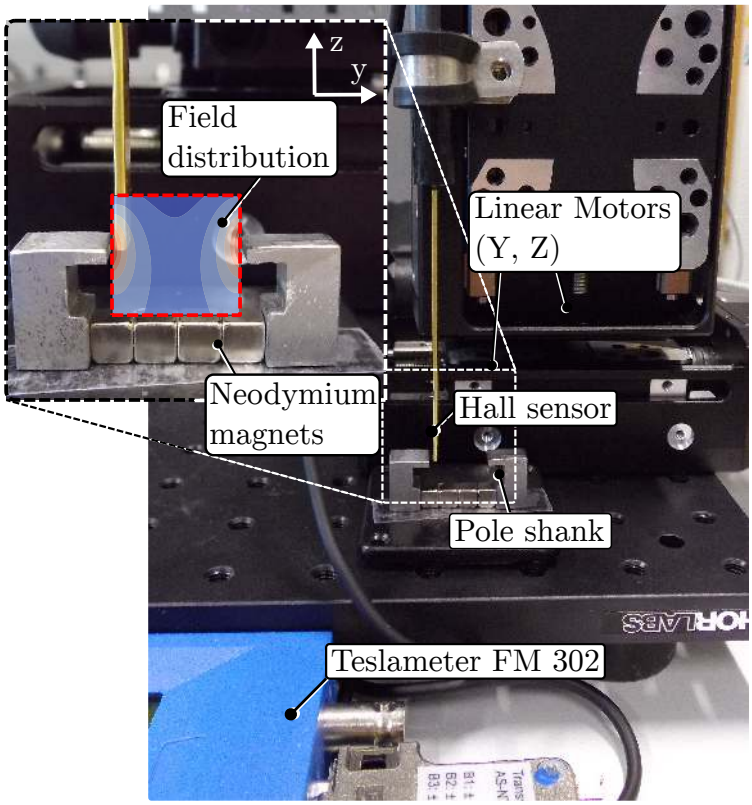

Figure 39: Measurement setup for the magnetic field characterisation among two pole shanks. A transversal Hall probe of type 'AS-NTM-2' was used to measure the B field distribution in the yz-plane (red frame).

References

[1] J. Lenz and S. Edelstein, "Magnetic sensors and their applications", *IEEE Sensors Journal*, 6(3), 2006, pp. 631–649.

[2] Agustín L. Herrera-May, et al., "Resonant Magnetic Field Sensors Based On MEMS Technology", *Sensors*, 9, 2009, pp. 7785–7813, URL `www.mdpi.com/journal/sensors`.

[3] Asaf Grosz, et al., "A High-Resolution Planar Hall Effect Magnetometer for Ultra-Low Frequencies", *IEEE SENSORS JOURNAL*, 16(9), 2016.

[4] O. Le Contel et.al., "The Search-Coil Magnetometer for MMS", *Space Sci Rev*, 166, 2016, pp. 257–282.

[5] Robert Bazinet, et al., "A Low-Noise Fundamental-Mode Orthogonal Fluxgate Magnetometer", *IEEE Transactions on Magnetics*, 50(5), 2013.

[6] John R. Brauer, *MAGNETIC ACTUATORS AND SENSORS*, John Wiley & Sons, Hoboken, New Jersey, 2nd edn., 2014.

[7] Agustín Leobardo Herrera-May, et al., "Recent Advances of MEMS Resonators for Lorentz Force Based Magnetic Field Sensors: Design, Applications and Challenges", *Sensors*, 16(1359), 2016, URL `www.mdpi.com/journal/sensors`.

[8] A L Herrera-May, et al., "A resonant magnetic field microsensor with high quality factor at atmospheric pressure", *Journal of Micromechanics and Microengineering*, 19(1), 2009, p. 015016, URL `http://stacks.iop.org/0960-1317/19/i=1/a=015016`.

[9] G. Langfelder, et al., "Z-Axis Magnetometers for MEMS Inertial Measurement Units Using an Industrial Process", *IEEE Transactions on Industrial Electronics*, 60(9), 2013, pp. 3983–3990.

[10] G. Laghi, et al., "Torsional MEMS magnetometer operated off-resonance for in-plane magnetic field detection", *Sensors and Actuators A: Physical*, 229, 2015, pp. 218 – 226, URL `http://www.sciencedirect.com/science/article/pii/S0924424715000369`.

[11] P. Minotti, et al., "A Sub-400-nT/ $\sqrt{\text{Hz}}$, 775- μW , Multi-Loop MEMS Magnetometer With Integrated Readout Electronics", *Journal of Microelectromechanical Systems*, 24(6), 2015, pp. 1938–1950.

[12] Byoungyoul Park, et al., "Lorentz force based resonant MEMS magnetic-field sensor with optical readout", *Sensors and Actuators A: Physical*, 241, 2016, pp. 12 – 18, URL `http://www.sciencedirect.com/science/article/pii/S0924424716300322`.

[13] Reza Abdolvand, et al., "Micromachined Resonators: A Review", *Micromachines*, 7(160), 2016, URL www.mdpi.com/journal/micromachines.

[14] Wilfried Hortschitz, *Hybrid MOEMS Displacement Sensor and Accelerometer: Sensing Concept, Design, and Technology*, Ph.D. thesis, 2013.

[15] W. Hortschitz et. al., "Novel MOEMS Lorentz Force Transducer for Magnetic Fields", *Procedia Engineering*, 168, 2016, pp. 680 – 683, URL http://www.sciencedirect.com/science/article/pii/S1877705816335597.

[16] Oliver Brand et al., *Resonant MEMS: Fundamentals, Implementation, and Application*, Wiley, April 2015.

[17] Wolfgang Demtröder, *Demtröder Experimentalphysik 1, Mechanik und Wärme*, Springer-Lehrbuch, vierte auflage edn., 2005.

[18] S. Schmid and C. Hierold, "Damping mechanisms of single-clamped and prestressed double-clamped resonant polymer microbeams", *Journal of Applied Physics*, 104(9), 2008, p. 093516, URL http://dx.doi.org/10.1063/1.3008032.

[19] Adalbert Prechtl, *Vorlesungen über die Grundlagen der Elektrotechnik*, vol. 2, Springer, 2007.

[20] Ian Ashdown, *Radiosity: A Programmer's Perspective*, Wiley, 1994.

[21] A. Kainz, et al., "Accurate analytical model for air damping in lateral MEMS/MOEMS oscillators", *Sensors and Actuators A: Physical*, 255, 2017, pp. 154 – 159, URL http://www.sciencedirect.com/science/article/pii/S0924424716312158.

[22] T. B. Gabrielson, "Mechanical-Thermal Noise in Micromachined Acoustic and Vibration sensors", *IEEE Trans on Electron Devices*, 40(5), 1993, pp. 903–909.

[23] www.osioptoelectronics.com OSI Optoelectronics, "Photodiode Characteristics", Catalog, 2017, URL www.osioptoelectronics.com.

[24] W. Hortschitz, et al., "Robust Precision Position Detection With an Optical MEMS Hybrid Device", *IEEE TRANSACTIONS ON INDUSTRIAL ELECTRONICS*, 59(12), 2012, pp. 4855–4862.

[25] Burr-Brown Corporation, "Design Photodiode Amplifier Circuits with OPA128", Application Bulletin, 1994.

[26] Veikko Lindroos, et al., *Handbook of Silicon Based MEMS Materials and Technologies*, ISBN : 978-0-8155-1594-4, William Andrew (is an imprint of Elsevier), 1st edn., 2010.

[27] Masaaki Kurihara et. al., "3D structural templates for UV-NIL fabricated with gray-scale lithography", *Microelectronic Engineering*, 84, 2007, pp. 999–1002.

[28] C.M. Waits, et al., "Microfabrication of 3D silicon MEMS structures using gray-scale lithography and deep reactive ion etching", *Sensors and Actuators A*, 119, 2004, pp. 245–253.

[29] Steve Simon Victor A. Lifton, Gregory Lifton, "Options for additive rapid prototyping methods (3D printing) in MEMS technology", *Rapid Prototyping Journal*, 20(5), 2014, pp. 403–412.

[30] Georg A. Reider, *Photonik, Eine Einführung in die Grundlagen*, Springer, 3rd edn., 2012.

[31] Joachim Fischer and Martin Wegener, "Three-dimensional optical laser lithography beyond the diffraction limit", *Laser Photonics Rev*, 7(1), 2013, pp. 22–44.

[32] Andreas C. Fischer, et al., "Chapter 26-Inkjet Printing, Laser-Based Micromachining and Micro 3D Printing Technologies for MEMS", in *Handbook of Silicon Based MEMS Materials and Technologies (Second Edition)*, edited by Tilli Markku et.al, William Andrew Publishing, Boston, Micro and Nano Technologies, second edition edn., 2015, pp. 550 – 564, URL `http://www.sciencedirect.com/science/article/pii/B9780323299657000269`.

[33] Christopher N. LaFratta, et al., "Multiphoton Fabrication", *Angewandte Chemie, International Edition*, 46(33), 2007, pp. 6238–6258.

[34] Ke Sun et al., "3D Printing of Interdigitated Li-Ion Microbattery Architectures", *Advanced Materials*, 25, 2013, pp. 4539–4543.

[35] Andreas C. Fischer et al., "Layer-by-Layer 3D Printing of Si Micro- and Nano structure s by Si Deposition, Ion Implantation and Selective Si Etching", in *12th IEEE Conference on Nanotechnology (IEEE-NANO)*, 2012.

[36] S.J. Leigh et al., "A miniature flow sensor fabricated by micro-stereolithography employing a magnetite/acrylic nanocomposite resin", *Sensors and Actuators*, 168, 2011, pp. 66–71.

[37] Reena Dahle and Rafiul Rasel, "3-D Printing as an Effective Educational Tool for MEMS Design and Fabrication", *IEEE TRANSACTIONS ON EDUCATION*, 59(3), 2016.

[38] Shapeways, "https://www.shapeways.com/materials/frosted-detail-plastic", , 2017, URL `https://www.shapeways.com/materials/frosted-detail-plastic`.

[39] I.Materialise, “https://i.materialise.com/”, , 2017.

[40] Thorlabs, “https://www.thorlabs.com/”, , 2017.

[41] micro lithography services, “http://www.microlitho.co.uk”, , 2017.

[42] DOTMAR plastic solutions, “http://www.dotmar.com.au/propertiestables.php”, , 2017.

[43] Silvan Schmid, *Electrostatically actuated all-polymer microbeam resonators Characterization and application*, Ph.D. thesis, ETH ZURICH, 2009, URL `https://doi.org/10.3929/ethz-a-005910629(September2017)`.

Code of Conduct

Hiermit erkläre ich, dass die vorliegende Arbeit gemäß dem Code of Conduct - Regeln zur Sicherung guter wissenschaftlicher Praxis (in der aktuellen Fassung des jeweiligen Mitteilungsblattes der TU Wien), insbesondere ohne unzulässige Hilfe Dritter und ohne Benutzung anderer als der angegebenen Hilfsmittel, angefertigt wurde. Die aus anderen Quellen direkt oder indirekt übernommenen Daten und Konzepte sind unter Angabe der Quelle gekennzeichnet.

Die Arbeit wurde bisher weder im In- noch im Ausland in gleicher oder in ähnlicher Form in anderen Prüfungsverfahren vorgelegt.

Wien,

Matthias Kahr